Prediction of flame structure and pollutant formation of Sandia flame D using Large Eddy Simulation with direct integration of chemical kinetics

Thomas Jaravel [a,b,*], Eleonore Riber [a], Bénédicte Cuenot [a], Perrine Pepiot [c]

[a] CERFACS, 42 Avenue Gaspard Coriolis, Toulouse Cedex 01 31057, France
[b] Safran Aircraft Engines, Moissy Cramayel 77550, France
[c] Sibley School of Mechanical and Aerospace Engineering, Cornell University, NY 14853, United States

ARTICLE INFO

ABSTRACT

Large Eddy Simulation (LES) with direct integration of reduced chemical kinetics including NO chemistry is performed on the Sandia flame D. This approach allows a detailed analysis of the flame structure and pollutant formation. The Analytically Reduced Chemistries (ARCs) are obtained using Directed Relation Graph method with Error Propagation (DRGEP) and Quasi-Steady-State (QSS) approximation. Two ARCs containing both 22 species are derived for methane–air oxidation, from GRI 2.11 and GRI 3.0 detailed mechanisms. They correctly predict fuel consumption speed, as well as NO and CO concentrations in laminar premixed and non-premixed flames at atmospheric conditions. It is found that the NO production strongly depends on the detailed mechanism, being significantly higher with GRI 3.0 in rich premixed flames and in diffusion flames. The two ARCs are then used in highly-resolved LES of the Sandia flame D. The numerical results are in very good agreement with the experiment in terms of aerodynamics, mixture fraction and temperature profiles. The CO concentration is also well predicted with the two ARCs. For NO, a satisfactory agreement with the measurements is obtained with the ARC based on GRI 2.11, while a significant over-prediction is obtained with the GRI 3.0-based ARC, consistently with the differences observed in laminar cases between the two GRI versions. A detailed investigation of the flame structure including a comparison with reference laminar flames reveals that the flame structure is essentially non-premixed. The presence of the pilot jet alters the mixing process, leading to a flame structure that falls between two extreme non-premixed combustion regimes corresponding to the interaction of the rich central jet with either the hot gases from the pilot, or the coflow of fresh air. The associated laminar diffusion flamelets indicate that this particular flame structure influences the formation of pollutants, with a strong impact on CO production.

1. Introduction

Stringent regulations of pollutant emissions apply to new-generation combustion devices. The development of aeronautical lean-premixed burners has led to a global reduction of NO_x emission levels, which is a major environmental concern. However, these new engine designs are generally operated close to the lean blow-off limit, which might result in increased carbon monoxide (CO) emissions, in particular at low-power conditions. CO is formed in the flame region from highly reactive precursors such as HCO. The oxidation of CO into CO_2 is a slower process, initiated in the flame zone and continuing in the post-flame region. As a consequence, high CO concentrations are found in fuel-rich conditions because of the lack of oxygen in the burnt gases for the oxidation into CO_2. High CO levels are also related to flame quenching that occurs for example by flame-wall interaction or by the presence of cooling air. In addition, close to lean blow-off conditions, incomplete oxidation of CO can occur if the residence time in the combustor is insufficient. All these effects may lead to CO concentration values significantly higher than equilibrium at the combustor exit. The chemistry of NO is significantly different, and follows several major chemical pathways. The thermal, N_2O and NNH routes [1–3] describe the interaction of the N_2 species with O and OH radicals, whereas the prompt NO route [4] is driven by the interaction with hydrocarbon radicals such as CH formed during the fuel oxidation process. In the flame region, thermal NO formation

is promoted by the super-equilibrium concentrations of O and OH radicals [3]. The prompt NO route is very significant in rich regions of the flame because of large concentrations of hydrocarbon radicals, but generally negligible in the burnt gas region where they are no longer present. In this region, the thermal route remains as the main contributor to NO formation. NO formation in burnt gases is one order of magnitude slower than in the flame region and is an exponential function of the temperature. Depending on residence time, temperature and pressure conditions, this slow post-flame process can account for 35–70% of the total NO formation [5]. As most practical combustion devices have very limited residence time, NO levels at the combustor exit remain largely below equilibrium values.

Even though CO and NO formation chemistry is rather well understood, the accurate prediction of CO and NO levels in real aeronautical configurations remains a challenge because they are strongly impacted by various effects such as multiphase combustion, turbulence, cooling and dilution air, as well as radiative and wall heat transfers. The high temperature environment and limited optical access make the measurement of chemical species very difficult inside the combustion chamber. Therefore, experimental data in real gas turbine burners are often limited to exhaust gas composition measurements, which does not allow for an exhaustive validation of models for pollutant formation and emissions. On the other hand, while they may not capture all phenomena occurring in real industrial chambers, academic configurations typically allow for more comprehensive measurement data sets against which models can be compared. Among others, the turbulent non-premixed Sandia Flame D, studied experimentally by Barlow and Frank [6], is of particular interest as a large amount of data is available for temperature, major species, and pollutant concentrations in the flame and post-flame regions. This configuration was extensively used as a validation case for pollutant formation modelling, as it contains some essential features of turbulence/chemistry interaction.

Most modelling effort for pollutant prediction in recent years relied on tabulated chemistry approaches, with the combustion process described using both premixed [7,8] and non-premixed flamelet manifolds [8–11]. Overall, a fair agreement was generally obtained between measurements and simulations of the main flame characteristics. However, the standard flamelet hypothesis is not appropriate to describe the slow processes of pollutant formation and model adjustments are required. Few efforts have been devoted to the development of specific models for CO formation. In the work of Vreman et al. [8], CO concentration was directly extracted from a chemical look-up table. In contrast to mixture fraction, temperature and major species predictions, CO prediction was found to be more sensitive to the choice of the manifold. A significant over-prediction of CO levels was obtained with a manifold based on premixed flames, which was reduced when using a non-premixed manifold. The NO mass fraction was not directly extracted from the flamelet manifold, but from an additional transport equation, still using a tabulated chemical source term, in order to correctly account for transport history effect. Because of the additional chemical time-scales introduced by the NO chemistry, the chemical state cannot be fully described by a single flame progress variable. Additional modelling effort is then required to tabulate NO chemistry with one or several additional progress variables. Pecquery et al. [7] showed that NO evolves along a low-dimensional manifold in the post-flame region, well described by the NO mass fraction as a progress variable. This was therefore employed for the tabulation of the NO source term in the post-flame region. No additional progress variable was used in the flame region. In a similar approach, Ihme and Pitsch [10] assumed a linear dependency of the NO source term on the NO mass fraction. In the work of Zoller et al. [11], this linearisation was replaced by the

time evolution of a perfectly-stirred reactor with frozen fuel oxidation chemistry to extract the NO source term as a function of the NO mass fraction. These various models led to reasonable NO prediction in academic configurations. However, a major limitation of tabulation-based models dedicated to CO and NO prediction is that their application to real configurations with complex flow and flame structures, including multiphysics phenomena such as heat transfer and spray combustion is not straightforward.

To overcome such limitations of tabulated chemistry approach, an alternative is to solve directly the chemical problem, integrating all species transport equations with their chemical source term. To limit the computational cost, reduced mechanisms are generally employed. Globally fitted reduced mechanisms with 2–4 reaction steps reproduce major quantities (e.g. flame consumption speed and temperature), but are not well-suited to predict pollutant formation as they do not include enough species. More advanced, knowledge-based reduction techniques allow to derive larger and accurate reduced mechanisms that preserve a faithful description of the flame structure, and can therefore handle multiple and complex combustion regimes in real configurations where pressure and temperature conditions may vary significantly. Such schemes will be referred to in the following as analytically reduced chemistries (ARCs), and typically contain 10–30 species depending on the fuel complexity and the inclusion of pollutant chemistry. For example, methane–air combustion is described with ARCs comprising 10–20 species [12,13] that have demonstrated their capability to accurately predict NO formation in canonical configurations such as perfectly stirred reactors, laminar freely propagating flames, and diffusion flames. Thanks to the continuous increase of computational power, ARCs have become tractable in large-scale unsteady problems, and have been recently applied to LES of turbulent flames, using various models for the subgrid interaction of chemistry and turbulence. A first family of models relies on solving statistical fields describing the local chemical state, based on the existence of a fine-grain probability distribution function describing the subgrid interaction of turbulence and chemistry. In the work of Jones and Prasad [14] on the Sandia Flame Series (D-F), and Bulat et al. [15] in a turbulent premixed swirled burner, this was done using the Eulerian stochastic fields method with a 19-species ARC. ARCs can also be coupled with the Conditional Moment Closure model, as done in [16]. Finally, an alternative approach is the artificially thickened flame model, which allows to resolve directly the chemistry on the grid. It was successfully applied to partially premixed swirled burners [17,18] and to autoignition stabilised jet flame [19].

As ARC allows a faithful description of the chemistry, the primary objective of this work is to demonstrate its potential to better predict and understand the flame structure and pollutant formation using this approach for the simulation of the Sandia flame D configuration. To alleviate the potential impact on the analysis of modeling assumptions related to subgrid turbulence–chemistry interaction, the choice is made to perform LES with a mesh sufficiently resolved to neglect the impact of subgrid turbulence-chemistry interaction. Still, it is not a Direct Numerical Simulation as subgrid turbulence remains to be modelled. To the best of the authors' knowledge, this is the first attempt to perform a LES of the Sandia flame D with direct resolution of a realistic chemical kinetics including NO chemistry.

In a first step, several ARCs for methane–air oxidation including CO and NO chemistry are derived from GRI detailed mechanisms [20,21] and evaluated on canonical one-dimensional problems, illustrating their accuracy and the sensitivity of the results to the choice of the detailed mechanism. In a second step, ARCs are employed in LES computations of the Sandia flame D, with direct resolution of the chemistry on the grid. After the prediction capability of the methodology being evaluated through comparison

with measurements of mixing, temperature, and pollutant concentrations, the chemical response to unsteady flow features in terms of flame structure and pollutant formation is further analysed and compared with reference flamelet solutions, giving new insight on the mechanisms of pollutant formation in this turbulent flame.

2. Derivation and validation of ARCs for methane–air oxidation including NO and CO chemistry

The reference detailed mechanism retained to describe methane oxidation and NO chemistry is the GRI mechanism. Recent studies [22,23] underline the central role of NCN species in prompt NO formation, whereas HCN is considered in GRI mechanism. Despite this limitation, this scheme has proven to yield satisfactory results in previous studies of the Sandia D flame and is retained here. The mechanism is available in two versions: GRI 2.11 [20] and GRI 3.0 [21]. The differences between them were highlighted by Cao and Pope [24] and Barlow et al. [25]. The main difference is the prediction of CH radical, which leads to a significantly higher prompt NO prediction by GRI 3.0. To allow a fair assessment, both versions of the GRI are considered here.

Example of derivation of reduced mechanisms for methane including NO chemistry can be found in [12,13], however they are based on GRI 3.0 only. Therefore a new reduction is performed here with both GRI versions. The objective of the reduction process is to simplify the chemical kinetic description while preserving the main chemical paths needed to predict the flame structure, response to turbulence, as well as NO and CO formation in a large range of conditions. A set of five laminar freely-propagating premixed flames, with equivalence ratios in the range $\phi = 0.6$–1.4, at atmospheric pressure and temperature is chosen as target dataset for the reduction process, which is performed with the YARC reduction tool [26]. For brevity, details are provided below for the reduction based on the GRI 2.11 only.

2.1. Skeletal reduction

The first step is to identify and remove the species and reactions that are of minor importance for the dynamic of the kinetic system. This is done here using the Directed Relation Graph with Error Propagation method (DRGEP) [27]. Starting from the GRI 2.11 mechanism, eight species, HCCOH, C_2H, CH_2CO, CH_2OH, CN, NH_3, H_2CN, and HCNN are removed, as well as the reactions involving these species. In addition, 114 unimportant reactions (note that forward and backward reactions are counted separately) are further removed to reduce the stiffness and the complexity of the mechanism. The resulting skeletal mechanism contains 40 species and 320 reactions. The maximum relative error introduced by this first reduction step is 3% for the laminar flame speed, 9% for CO and 6% for NO burnt gas mass fractions, as evaluated over the whole set of target flames.

2.2. Quasi-steady state approximation

The size and complexity of the skeletal mechanism is further reduced using the Quasi-Steady State (QSS) approximation. QSS species concentrations are obtained from an algebraic system of equations, and do not require anymore to solve a transport equation, resulting in substantial computational time savings. Also, since QSS species are typically highly-reacting intermediates associated with small temporal and spatial scales, the chemical stiffness of the mechanism is reduced [28].

The appropriate QSS species are identified using a Level Of Importance criterion [29,30]. Most intermediate species related to NO chemistry (N, NH, NNH, HNO, NH_2, NCO, HCNO, HNCO, HOCN) are found to be good candidates for QSS approximation. HCN and

N_2O species, which are related respectively to the prompt NO and N_2O chemical pathways, as well as the final products of the NO chemistry (NO and NO2) are kept as transported species. For the methane oxidation part, 9 species, namely C, CH, CH_2, $CH_2(S)$, HCO, CH_3O, C_2H_3, C_2H_5, and HCCO are retained for QSS approximation. Explicit analytical expressions are derived for the concentrations of QSS species from the algebraic QSS system. Finally, 22 non-QSS species remain in the resulting ARC, called ARC_22_GRI211 in the following. Compared to GRI 2.11, the maximum relative error of ARC_22_GRI211 is 5% for the laminar flame speed, 8% for CO and 2% for NO species burnt gas mass fractions on the set of target flames.

The exact same methodology is applied to the GRI 3.0 mechanism, resulting in a second reduced scheme, called ARC_22_GRI30. This mechanism contains the same 22 transported species as ARC_22_GRI211. The set of QSS species is identical to that of ARC_22_GRI211, except for additional species, namely CN, H_2CN, and CH_2OH, that were discarded in ARC_22_GRI211, but are retained in ARC_22_GRI30. Compared to GRI 3.0, the maximum relative error of ARC_22_GRI30 is 7% for laminar flame speed, 10% for CO and 9% for NO species burnt gas mass fractions for the set of target flames.

The resulting ARCs are similar to previous works including NO chemistry [12,13] based on GRI 3.0, despite differences in the choice of the target applications for reduction. In the work of Lu and Law [13], the reduction was based on autoignition and perfectly-stirred reactor test cases, leading to a similar reduced mechanism. At the exception of CH_2CO and CH_2CHO, which are discarded in the present work, the retained transported and QSS species are the same. Regarding NO chemistry, the N_2O pathway for NO and NO_2 formation are accounted for in ARC_22_GRI30, while they were discarded in the reduction of Lu and Law, and more intermediates related to prompt NO formation are retained. On the overall, the two mechanisms are relatively close and are both suitable for the target applications considered here. In the work of Sung et al. [12], the O atom was considered as a Quasi-Steady-State (QSS) species, whereas it was found in the present study that this alone would lead to errors up to 20% for the quantities of interest. The main difference in terms of methodology is that NO chemistry is included from the beginning and reduced simultaneously with the fuel-oxidation chemistry in this work, whereas NO chemistry was only considered after the reduction of the fuel-oxidation part in the two previous studies. Because of the strong coupling of NO formation with carbon radicals in the flame region, this may significantly impact the overall prediction capability of the reduced mechanism. To illustrate the impact of including NO chemistry from the start in the reduction process, a third mechanism is derived from the GRI 2.11 without consideration of NO chemistry. If the accuracy requirements for rich conditions ($\phi > 1.2$) are removed, 11 additional species related to methane–air oxidation can be removed compared to ARC_22_GRI211: H_2O_2, CH_3OH, C_2H_2, C_2H_4, C_2H_6, C, CH, CH_3O, C_2H_3, C_2H_5 and HCCO. The NO chemistry is included after the additional reduction step, by adding the same QSS and transported nitrogen species as in ARC_22_GRI211. The resulting mechanism comprises 17 transported species, and is named ARC_17_GRI211 in the following.

3. Assessment of ARCs on laminar flames

The target turbulent Sandia flame D exhibits a complex structure where non-premixed combustion regime is dominant, but premixed combustion can also occur locally [7]. Therefore the reduced mechanism must be able to describe both regimes. The set of test flames retained for the reduction process ensures that the reduced mechanisms behave correctly in the premixed combustion

(a) Temperature profile.

(b) CO and NO mass fraction profiles.
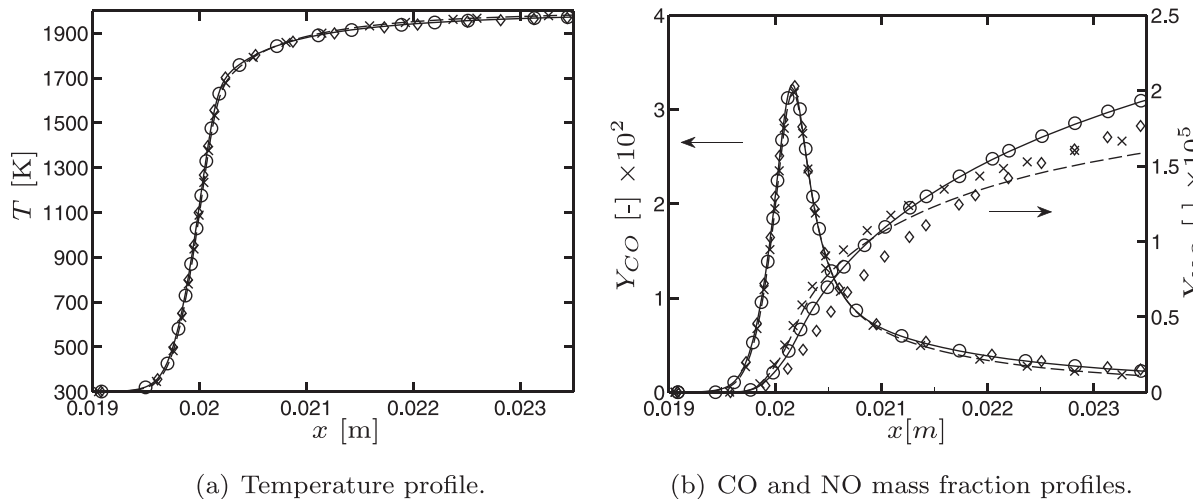
Fig. 1. One-dimensional premixed unstrained flame at an equivalence ratio $\phi = 0.8$. Comparison between GRI 2.11 (−), ARC_22_GRI211 (○), ARC_17_GRI211 (◇), GRI 3.0 (−−), ARC_22_GRI30 (×) in terms of a) temperature and b) CO and NO mass fractions.

(a) Temperature profile.

(b) CO and NO mass fraction profiles.
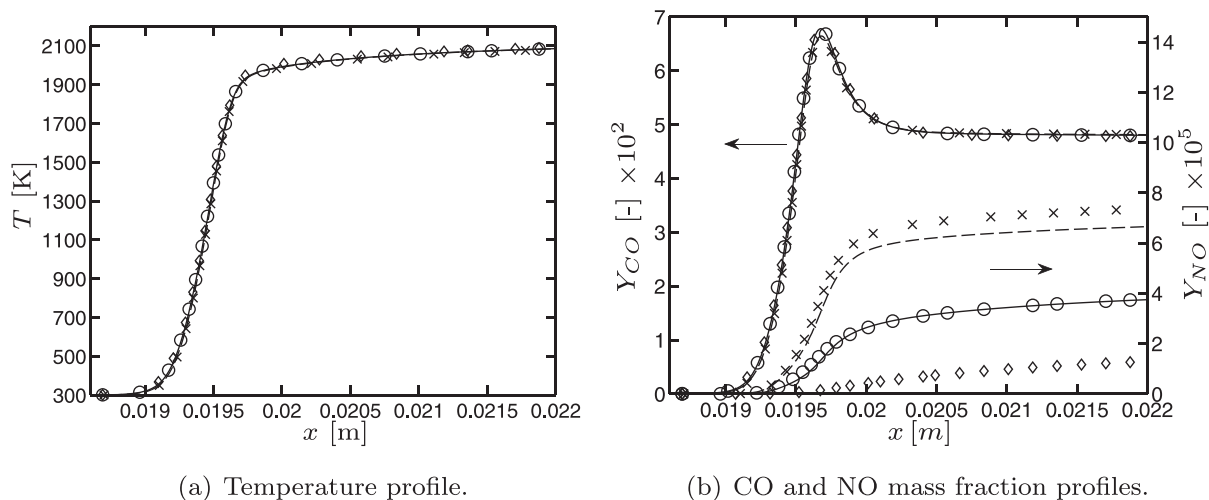
Fig. 2. One-dimensional premixed unstrained flame at an equivalence ratio $\phi = 1.2$. Comparison between GRI 2.11 (−), ARC_22_GRI211 (○), ARC_17_GRI211 (◇), GRI 3.0 (−−), ARC_22_GRI30 (×) in terms of a) temperature and b) CO and NO mass fractions.

regime. The prediction capability of the resulting reduced mechanisms in the non-premixed combustion regime is also to be assessed on canonical non-premixed flames.

3.1. Analysis of laminar unstretched premixed flames

The behaviour of ARCs derived in Section 2 is first analysed on the one-dimensional laminar unstrained premixed flames used in the reduction process. The solutions obtained with the three ARCs are shown in a lean case at $\phi = 0.8$ (Fig. 1) and a rich case at $\phi = 1.2$ (Fig. 2). In both cases, all detailed and reduced mechanisms exhibit the same profiles of temperature and CO mass fraction, with a well-captured peak. Differences however appear on the NO mass fraction profiles, with stronger deviations observed in the rich case. In the lean case, the NO mass fraction increases at a rate that is of the same order of magnitude in the flame and in the post-flame regions, and the disparities between the two detailed mechanisms are small. The ARC_22_GRI211 scheme matches perfectly GRI 2.11, while a slight underprediction is observed with the ARC_17_GRI211. The ARC_22_GRI30 scheme slightly overpredicts GRI 3.0. Overall, the three reduced mechanisms ex-

hibit satisfactory NO prediction in the lean case. In the rich case ($\phi = 1.2$), the NO profile exhibits a change of slope, in contrast with the lean case. This indicates a switch from rapid prompt NO formation in the flame region to slower NO formation in the burnt gases. NO levels in the burnt gases are twice as high for GRI 3.0 compared to GRI 2.11. This discrepancy is attributed to the increased production of prompt NO in GRI 3.0. Overall, the agreement is very good between ARC_22s and their associated detailed mechanisms. In contrast, the ARC_17_GRI211 scheme largely underestimates the NO levels: the formation in the burnt gases is reproduced with the correct slope, indicating that the slow chemical processes are correctly captured, but the rapid increase of NO in the flame region is entirely missed. This is attributed to missing radicals in the reduced scheme such as CH, which are strongly involved in prompt NO formation.

To assess the global performance of the reduced mechanisms, the main properties of interest, namely laminar flame speed, and NO and CO formation rates integrated through the flame (i.e. production rate in the flame region) are shown as function of the equivalence ratio ($\phi = 0.6$–1.6) in Fig. 3. NO and CO flame production rates are obtained by integration of their respective source

(a) Laminar flame speed.

(b) NO production rate.

(c) CO production rate.
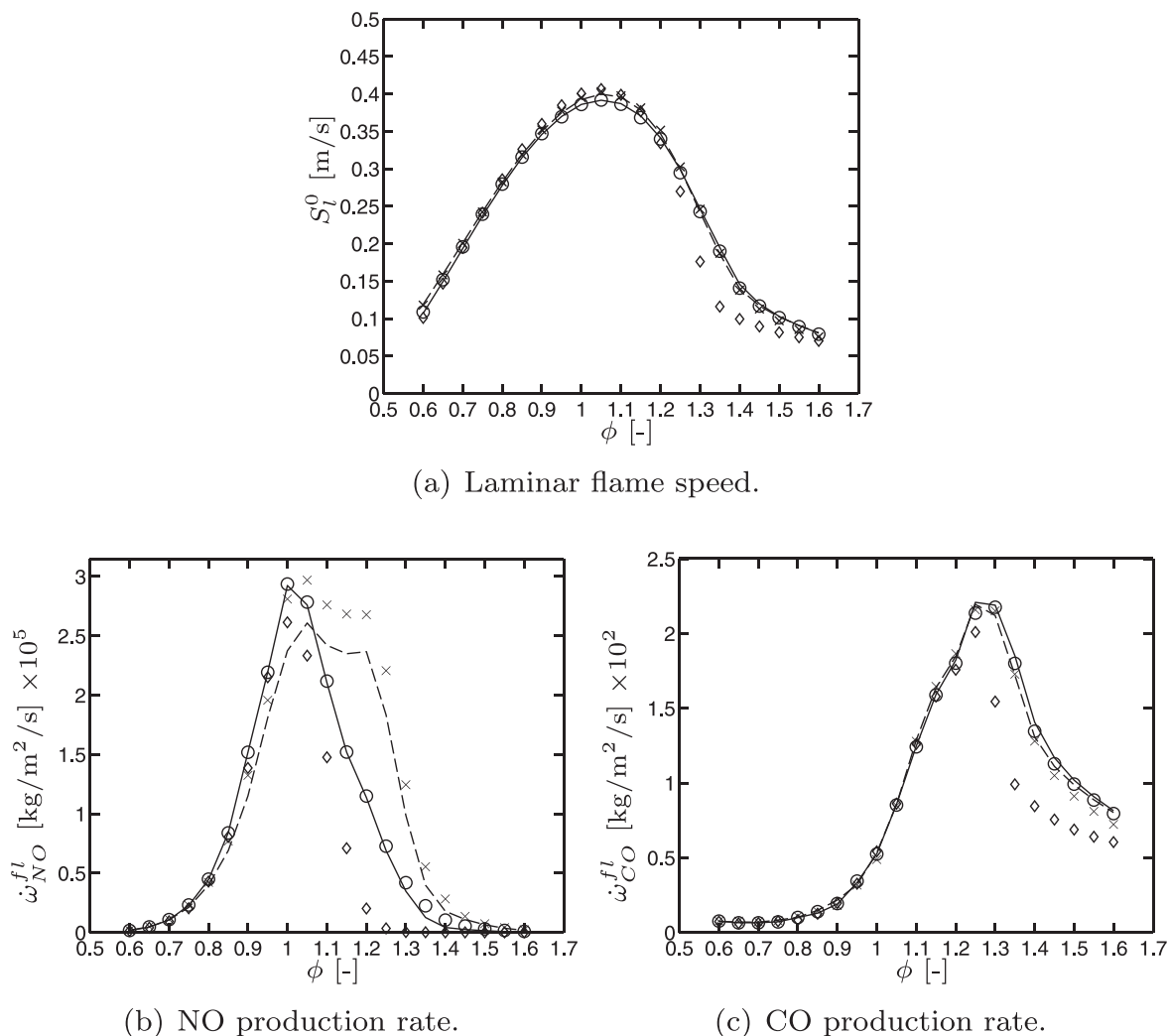
Fig. 3. One-dimensional unstrained premixed flames. Comparison between GRI 2.11 (−), ARC_22_GRI211 (○), ARC_17_GRI211 (◇), GRI 3.0 (−−), ARC_22_GRI30 (×) in terms of a) flame speed, b) NO and c) CO flame production rates as functions of the equivalence ratio.

term up to a given value of the progress variable $c = (Y_{CO} + Y_{CO_2} + Y_{H_2O})/(Y_{CO}^{eq} + Y_{CO_2}^{eq} + Y_{H_2O}^{eq})$, with the superscript eq denoting equilibrium values. The value $c = 0.98$ is used to delimit the flame region. It is sufficiently high to capture CO and NO formation in the flame reaction zone and sufficiently low to exclude the slow post-flame chemical processes. From Fig. 3, it can be seen that the ARC_22s recover well the laminar flame speed, and NO and CO flame production rates for the whole range of equivalence ratios considered, with only a slight over-prediction of NO production rate by ARC_22_GRI30, by about 10% in the range $\phi = 1$–1.2. The ARC_17_GRI211 also leads to very satisfactory results in terms of laminar flame speed and CO flame production rate up to $\phi = 1.2$, but poorly captures prompt NO, leading to a deterioration of NO prediction above $\phi \simeq 1.05$.

3.2. Validation on strained partially premixed flames

The reduced mechanisms are further validated on a series of strained counterflow partially-premixed flames that were not included in the reduction target cases, but are relevant for the intended LES application. As will be further described in Section 4.1, the Sandia flame D configuration comprises three inlets: a cold main jet of rich methane–air mixture, a hot pilot of lean burnt

gases, and an air coflow at ambient conditions, with detailed properties given in Table 1. To be representative of the target application, the present counterflow computations performed in physical space use the coflow jet composition and temperature conditions on one side of the one-dimensional domain, and the main jet composition and temperature on the other side, as provided in Table 1. It was shown that depending on the fuel side equivalence ratio ϕ_{fuel}, the flame structure switches from a double premixed/non-premixed flame to a single diffusion flame [31]. In the present case, ϕ_{fuel} is far off the rich flammability limit, which is around $\phi_{lim} = 1.85$, and only a simple diffusion flame exists. It should be noted that this configuration has been used to tabulate the chemistry in several previous LES studies of the Sandia flame D [8,10,11]. This series of flames with various strain rates is referred to as the coflow flamelet series hereafter.

The response to strain is assessed by varying the inlet velocities. To facilitate the comparison with the turbulent cases, the characteristic time scale associated with the strain rate acting on the flame is evaluated via the scalar dissipation rate, and is defined as

$$\chi = \chi_{Z=0.4} = \left(2D_{th} \mid \nabla Z \mid^2\right)_{Z=0.4} \tag{1}$$

where D_{th} is the thermal diffusivity and Z is the mixture fraction based on the carbon atom, normalised to be equal to 0 in

Table 1
Composition (mass fractions) and temperature of the three inlets of the Sandia flame D.

	$T[K]$	Y_{CH_4}	Y_{O_2}	Y_{CO_2}	Y_{H_2O}	Y_{CO}	Y_{NO}	ϕ
Main	294	0.156	0.197	0	0	0	0	3.17
Pilot	1880	0	0.054	0.111	0.0942	4×10^{-3}	2×10^{-5}	0.77
Coflow	291	0	0.230	0	0	0	0	0

(a) Maximum temperature.

(b) Total fuel consumption rate.

(c) Total CO production rate.

(d) Total NO production rate.
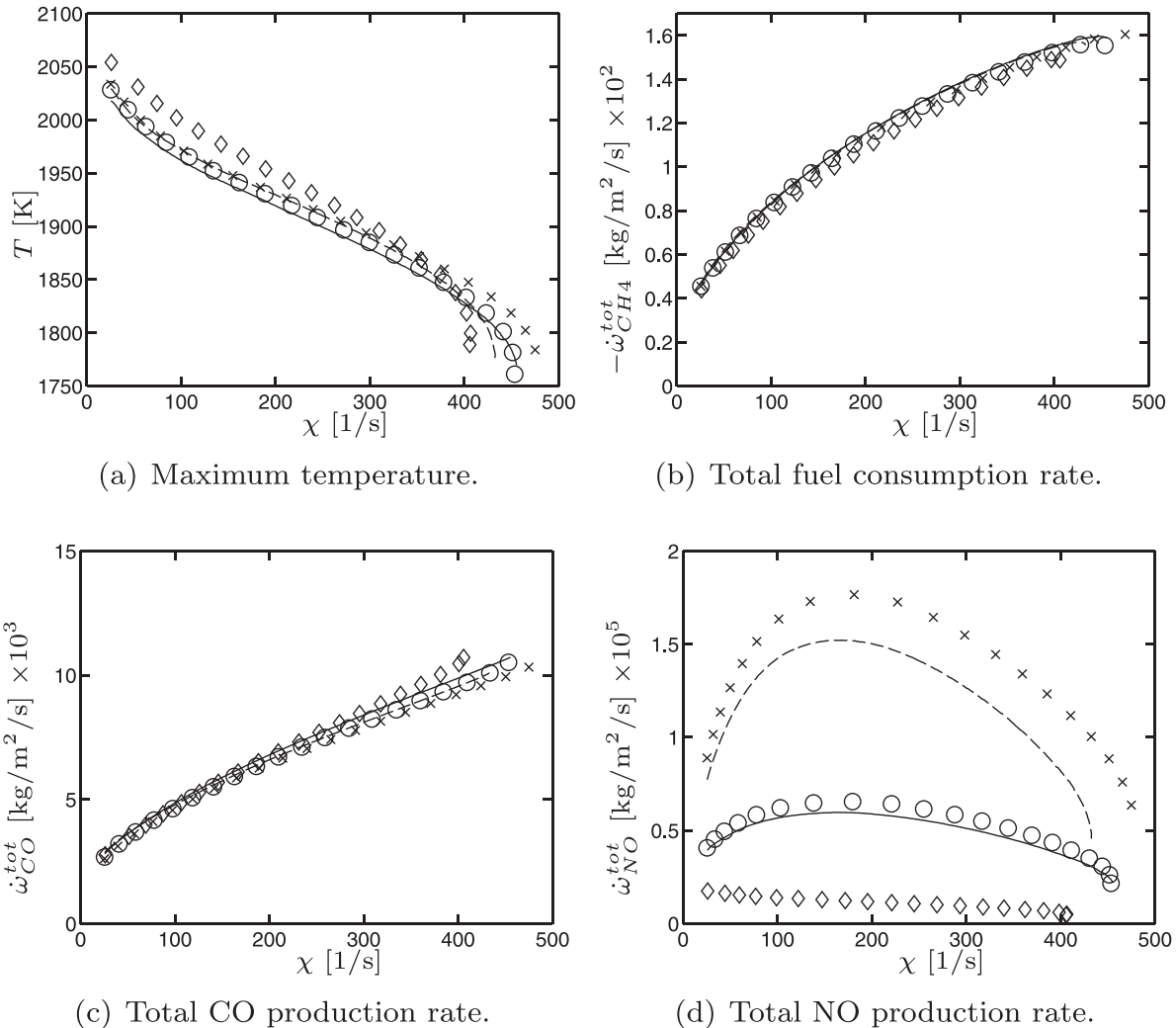
Fig. 4. Laminar coflow counterflow flames. Comparison of the response to the scalar dissipation rate χ between GRI 2.11 (—), ARC_22_GRI211 (○), ARC_17_GRI211 (◇), GRI 3.0 (– –), ARC_22_GRI30 (×), in terms of a) maximum temperature, b) CH_4 total consumption rate, c) total CO production rate and d) total NO production rate.

the air coflow and to 1 in the main jet, with stoichiometric value $Z_{st} = 0.351$. The choice $Z = 0.4$ rather than the more commonly used value $Z = Z_{st}$ is made based on the observation that the re-action zone with significant chemical source terms is located close to this value in mixture fraction space, as will be highlighted by the flame structures of Section 4.4.1. The response of the different mechanisms to the scalar dissipation rate is shown in Fig. 4. Note that the maximum scalar dissipation rate ($\chi \simeq 450s^{-1}$) corresponds to the extinction limit. The total fuel consumption rate and total CO formation rate exhibit a monotonic behaviour, well reproduced by all reduced mechanisms, and consistent with observations in premixed flames. The maximum temperature is also well recovered by all reduced schemes, except for ARC_17_GRI211 which exhibits higher deviations.

The response of NO total production rate to scalar dissipation rate is more complex, and differs strongly between the different

schemes. It first increases with scalar dissipation rate up to a maximum, then slowly decreases. The conclusions from the premixed cases in terms of differences between the mechanisms still hold: the NO production levels of ARC_22_GRI30 are overestimated by 10–15% compared to GRI 3.0 and GRI 2.11 yields NO formation rates significantly lower than GRI 3.0, and matched fairly well by ARC_22_GRI211. This is consistent with the findings of Barlow et al. [25], who performed a comparison of GRI 3.0, GRI 2.11, and experiments on this counterflow configuration. They found that the NO concentration peak in the flame region was overpredicted by a factor of 2 for GRI 3.0, whereas only a slight overprediction of the peak value was observed with GRI 2.11, which yielded the better overall agreement. In contrast, ARC_17_GRI211 strongly underestimates the NO production for the whole scalar dissipation rate range. It may be attributed to the absence of CH in ARC_17_GRI211, which largely controls prompt NO formation. To confirm this
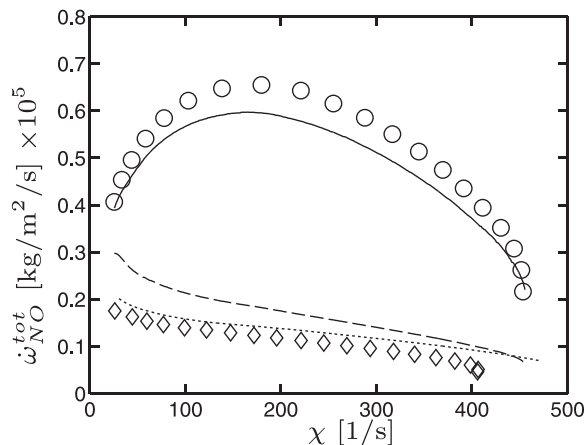
Fig. 5. Laminar coflow counterflow flames. Comparison of the response of total NO production rate to the scalar dissipation rate χ between GRI 2.11 $-$, ARC_22_GRI211 $\circ$, ARC_17_GRI211 $\diamond$, GRI 2.11 without prompt pathway $--$ and GRI 2.11 without CH species $\cdots$.

hypothesis, the original GRI 2.11 is modified in two ways: in one case, reactions related to prompt NO are removed (GRI 2.11 without prompt), and in the other only CH is discarded from the mechanism (GRI 2.11 without CH). The impact of these two modifications is shown in Fig. 5. The total NO formation is strongly reduced by the absence of prompt NO, which is a significant contributor in these types of flame. CH being a main precursor in the prompt NO pathway, discarding CH from the detailed mechanism has a similar effect. In both cases, the resulting total NO production levels are close to ARC_17_GRI211. This shows the strong impact of removing CH in the reduction process of the ARC_17_GRI211, and demonstrates the importance of including NO chemistry from the start in the derivation of the reduced mechanism.

In the following, since ARC_22_GRI211 and ARC_22_GRI30 exhibit very satisfactory agreement with their respective reference detailed mechanisms, but also very different NO prediction, both are retained for the numerical study of the Sandia flame D. Because of its poor prediction of NO production, ARC_17_GRI211 is not considered in the rest of the study.

4. LES of the Sandia flame D

4.1. Experimental configuration

The Sandia flame D is a turbulent jet flame studied experimentally by Barlow and Frank [6]. The burner consists of three coaxial jets. The main central jet is injected through a pipe of diameter $D = 7.2$ mm with a bulk velocity of 49.6 m/s. Its composition is a rich methane–air mixture, with an equivalence ratio of $\phi = 3.17$, at ambient conditions. The flame is stabilised via a pilot flow encompassing the main jet, with a bulk velocity of 11.4 m/s. It consists of burnt gases at an equivalence ratio $\phi = 0.77$. A coflow of air at ambient conditions is injected at 0.9 m/s and surrounds the pilot jet. As previously mentioned, the retained values for inlet compositions and temperatures are given in Table 1.

This configuration is particularly well-documented and is a reference case for NO model validation. Raman–Rayleigh measurements of species and temperature were performed by Barlow and Frank [6] at several axial locations, namely 1, 2, 3, 7.5, 15, 30, 45, 60 and 75D from the main jet exit. The estimated uncertainties are 3% for temperature, 5% for major species and 15% for NO concentration. Two-component Laser Doppler Velocimetry (LDV) measurements are also available for the same measurement planes.

4.2. Numerical setup

LES is performed using the AVBP solver co-developed by CERFACS and IFPEN, which solves the filtered fully compressible multispecies Navier–Stokes equations on unstructured grids. The TTGC centered spatial scheme from the continuous Taylor–Galerkin family [32] is used. This scheme has explicit time advancement and is third order accurate in both space and time. The three inlets and the outlet are described by Navier–Stokes Characteristic Boundary Conditions (NSCBC) [33] to ensure proper treatment of acoustics. The computational grid is fully unstructured and comprises 375 million tetrahedral elements. The full domain is 1 m long, with an outer diameter of 0.29 m. It includes a 10 mm long portion of the inlet ducts. The characteristic element size is $\Delta x = 90 \, \mu$m in the injection tubes and in the flame region up to the axial position $z = 3D$. Downstream of this axial position, the grid is linearly stretched to reach a characteristic size $\Delta x = 150 \, \mu$m at $z = 7.5D$, which is kept further downstream. The time step imposed by the acoustic CFL condition is $\Delta t = 16$ ns. This low value enables direct explicit integration of the chemical source terms of the two ARCs employed. Transport properties are obtained using a power-law for viscosity, a constant Prandtl number and a constant Schmidt number for each species, which are provided as supplementary material. It was verified that these simplifying assumptions have a minor impact on the laminar cases presented above.

4.2.1. Flame–turbulence interaction

The Kolmogorov length scale, estimated a priori as $\eta_\kappa ml_t Re_t^{-3/4}$ [34], where Re_t is the turbulent Reynolds number and l_t is the integral length scale, is found here in the range $\eta_\kappa \simeq 15 - 45 \, \mu$m, with l_t based on the main jet diameter and the turbulent intensity u' based on measured rms (root mean square) velocity at the main jet exit. In the flame region, the ratio of the grid size Δx to the Kolmogorov length scale η_κ falls in the range $\frac{\Delta x}{\eta_\kappa}m2$–6. Thus, the unresolved scales are expected to represent a very small part of the total fluctuating energy. This is supported by the very small values of the subgrid turbulent viscosity obtained with the SIGMA eddy viscosity model [35] in the LES (Fig. 7), except in the central core of the main jet where the subgrid turbulent viscosity is of the order of the laminar viscosity. In addition, numerical studies of chemical response of laminar methane–air diffusion flames to unsteady strain rate by Im et al. [36] indicate that the response of the flame structure to high-frequency fluctuations (typically beyond 1000 Hz) is rapidly suppressed. The lifetime of subgrid turbulent structures can be estimated as

$$\tau_{\Delta x} = u_{\Delta x}^{'2}/\epsilon \tag{2}$$

where $u_{\Delta x}^{'2}$ is the subgrid kinetic energy at the filter scale Δx, and ϵ is the rate of energy dissipation, which scales under the turbulent energy cascade assumption as [34]

$$\epsilon \propto \frac{u_{\Delta x}^{'3}}{\Delta x} \simeq \frac{u'^3}{l_t}. \tag{3}$$

By combining the two above equations, the typical lifetime is found to be $\tau_{\Delta x} = 0.1$ ms, which corresponds to a characteristic frequency $f_{\Delta x} = 10000$ Hz. According to Im et al. [36] and Cuenot et al. [37], such high-frequency fluctuations do not interact with the flame which has a much higher characteristic time scale ($\tau_{fl} \simeq 1$ ms). Based on these observations, the sub-grid flame–turbulence interaction can be neglected. It was also verified on two-dimensional counterflow flames that the retained grid resolution is sufficient to correctly resolve the chemical structure of the flame front at any strain rate below the extinction limit.

4.2.2. Turbulent flow injection and wall treatment

The theoretical velocity profile corresponding to a turbulent pipe flow at Reynolds number $Re = 22,400$ is imposed at the inlet of the main injection tube. Velocity fluctuations are superimposed with a turbulent intensity of $u' = 2$ m/s. This flow injection allows to recover the experimental mean and rms velocity profiles at the first axial measurement location $x/D = 1$. Note that the turbulent boundary layer is not resolved ($\Delta x \sim 0.09$ mm near walls, i.e. $y^+ = 10$) and a slip velocity condition is applied at the injection tube walls and at the outer border of the coflow.

4.2.3. Thermal conditions

As NO formation is very sensitive to temperature, special care must be taken when considering thermal effects. An *a posteriori* evaluation of the heat losses due to thermal radiation using the optically-thin-limit model described in [38] showed that they represent only 3% of the total heat release rate in the volume between the jet exits and the axial location $z = 30D$. Previous numerical studies [10,11] of the Sandia flame D also suggested that radiative effects have a very limited impact on temperature and major species in this flame. The impact on NO formation remained limited as well, with no significant impact before $z = 40D$ and a reduction of about 10–20% afterwards. Based on these observations, radiative heat losses are not considered in the present work. In addition, the walls are considered to be adiabatic.

4.2.4. Averaging procedure

The flow-through time, based on the bulk velocity of the main jet and the distance between the exit of the injection tube and the axial location $z = 30D$, is about 4.3 ms. Statistics were therefore collected over 15 ms for the ARC_22_GRI211 case, and over 8 ms for the ARC_22_GRI30 case, corresponding to 3.5 and 1.9 flow-through times, respectively. In addition, azimuthal averaging is applied when considering radial distributions of mean and root-mean-square (rms) quantities.

4.2.5. Computational cost

The computational cost for one flow-through time is 500,000 CPU hours on the CERFACS in-house NEMO cluster (Intel Haswell architecture). This high computational cost is essentially related to the fine grid resolution and small time-step of the simulation. Using reduced chemistry contributes to make the simulation tractable in two ways. First the number of transport equations to solve is reduced by a factor 2 with ARC compared to detailed GRI mechanism, reducing the total cost by a similar factor. Second, the QSS approximation reduces the stiffness of the chemical system, allowing to keep explicit time integration using the time step imposed by the CFL condition. Thus the chemical source terms are only evaluated once per iteration, representing 15% of the total simulation cost with ARC in this case. Using detailed GRI mechanism, stiff integration with multiple source term evaluations per time step would be required, dramatically increasing the overall computational cost [28].

4.3. Numerical results

The ARC_22_GRI211 and ARC_22_GRI30 mechanisms were found to yield almost identical LES results. Thus, they are presented as "ARC_22" without distinction, except for quantities related to NO for which differences between the two mechanisms are observed.

Instantaneous snapshots of mixture fraction, temperature, and CO and NO mass fraction fields in the mid-plane are shown in Fig. 6. The mixing layers between the 3 jets develop, generating turbulent structures that grow and lead to jet opening. The shear layer between the pilot jet and the main jet destabilises faster than the shear layer between the coflow and the pilot jet, as indicated by the larger amount of fine-scale structures. Note that isolated pockets of high NO concentrations are observed between $z = 15D$ and $z = 30D$ already, coinciding with regions of high temperature, whereas CO concentrations are high in the rich core of the jet.

The ratio of subgrid turbulent to laminar viscosity is commonly used to estimate *a posteriori* the ratio of resolved to unresolved scales. Figure 7 shows a scatter plot of this ratio at axial locations $z = 7.5D$ and $z = 15D$ as a function of the mixture fraction, where Z_{st} marks the location of the flame region. At its maximum, the subgrid turbulent viscosity is of the order of the laminar viscosity in the central region of the jet, where the mixture fraction Z is close to 1, and is 10 times smaller than the laminar value around stoichiometry. Based on this quantity, a rough estimate of the ratio of the filtering scale to the Kolmogorov scale can be obtained as $\Delta x / \eta_\kappa = (\nu_{turb}/\nu_{lam})^{1/2}/C_s$, where $C_s^2 = 0.032$ [39]. In the present case, this gives $\Delta x / \eta_\kappa$ m 5.6 in the central core, which is close to the *a priori* estimation given in Section 4.2.1. In the range $Z = 0.2$–0.6, where the reaction layer is located, the turbulent viscosity is found to be negligible, thus validating the assumption of neglecting the unresolved turbulence-chemistry interactions.

4.3.1. Velocity profiles

A very good agreement is obtained between LES results and experiments for the radial profiles of the mean axial velocity at the different axial locations (Fig. 8). The mean velocity gradient in the shear layer between the main and the pilot jets is well captured even if it is slightly shifted radially towards the central axis. The error ranges between 3% and 10%, whereas the uncertainty on the inlet axial velocity is 4% in the experiment. It is slightly more pronounced close to the centerline for axial positions in the range $z = 3D$–15D.

The rms axial velocity, shown in Fig. 9, are also in good agreement with the experimental data. Some discrepancies appear in the first measurement plane, where the rms values are underestimated in the exit region of the central main jet, i.e at $r/D = 0$–0.6. This may be a consequence of the flow injection with slipping velocity at walls. However, the axial velocity rms levels are rapidly recovered at the measurement planes located downstream. As it follows the radial position of the shear layer, the peak of the fluctuations slightly shifts radially towards the centre.

4.3.2. Mixture fraction and temperature profiles

The axial mean mixture fraction profile along the centerline is shown in Fig. 10(a). The evolution of the mixture fraction is well captured overall, despite a slight over-prediction of mixing downstream of the axial position $z = 20D$. A grid convergence study performed by Pecquery et al. [7] showed that this kind of discrepancy was reduced with increasing grid resolution, but was still present when using a similar grid size. Likewise, the axial mean temperature shown in Fig. 10(b) is slightly over-predicted downstream of the axial position $z = 10D$, which is consistent with the mixture fraction profile. The magnitude of mixture fraction and temperature fluctuations, shown in Fig. 11, are in good agreement with the experiment, except at the first location downstream of the injection tubes, where fluctuations of the mixture fraction is still close to 0 in the LES whereas they are already significant in the experiment. Note, however, that this non-zero rms value for the mixture fraction contradicts the almost zero temperature fluctuation measured at the same location. Radial profiles of the mean mixture fraction and temperature at the different locations, shown in Fig. 12 and in Fig. 13 respectively, are also in good agreement with the experimental data except at location $z = 30D$ where the profile is too flat close the center, which is consistent with the discrepancy observed in the evolution of the mixture fraction along the centerline.
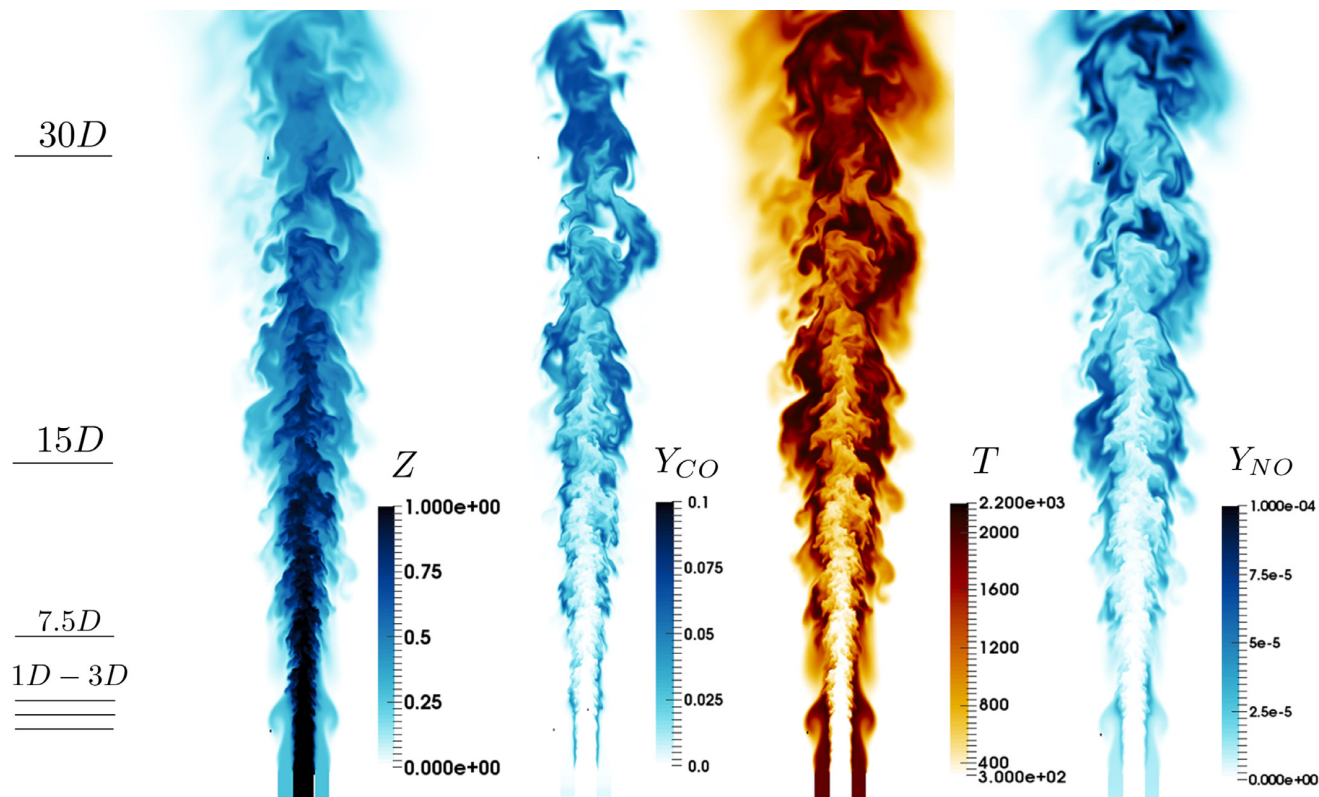
Fig. 6. Sandia flame D. Instantaneous fields in the mid-plane of mixture fraction (left), temperature (middle) and NO mass fraction (right) for ARC_22_GRI211. The measurement axial locations are indicated on the left.

(a) Axial position $z = 7.5D$. (b) Axial position $z = 15D$.
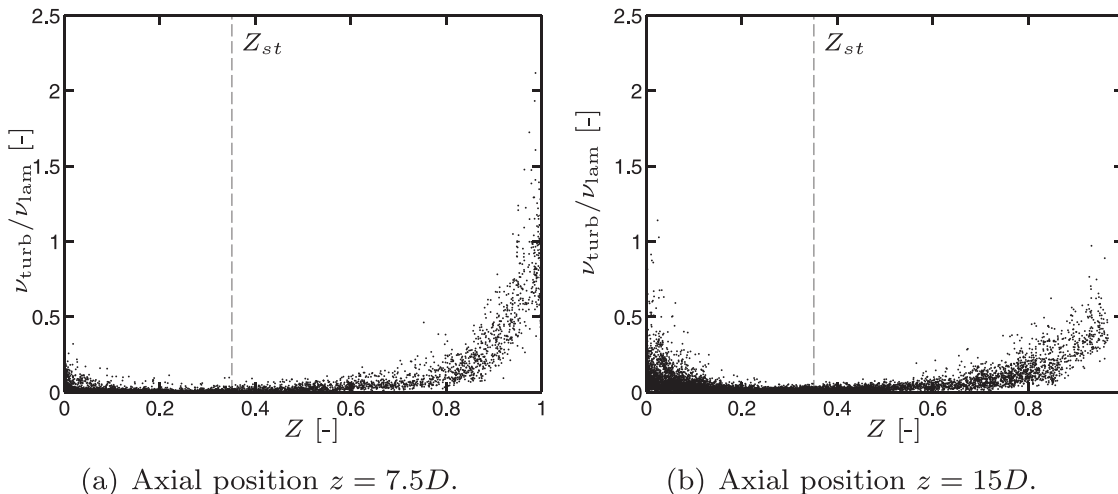
Fig. 7. Sandia flame D. Scatter plot of the ratio of sub-grid turbulent to laminar viscosity vs mixture fraction at axial locations $z = 7.5D$ and $z = 15D$.

4.3.3. NO and CO profiles

Figure 14(a) shows that the mean CO mass fraction along the centerline is well captured by both reduced schemes. The slight overprediction is related to the similar overprediction of the mixing on the centerline in Fig. 10(a). The mean CO mass fraction radial profiles of Fig. 15 reveal also a very good agreement with the experiment and in particular a good prediction of the peak in the reactive zone.

The situation is different for NO, for which the two versions of the reduced mechanisms are now distinguished. As shown in Fig. 14, the axial evolution of the mean NO mass fraction is well reproduced by ARC_22_GRI211, while ARC_22_GRI30 leads to significantly higher values for axial positions downstream $z = 15D$. The NO radial profiles at axial positions between $z = 1D$ and $z = 7.5D$ shown in Fig. 16 indicate that the NO peak value in the reaction zone is overestimated with ARC_22_GRI30, whereas ARC_22_GRI211 tends to underpredict it with similar deviation. Further downstream, a significant overprediction of NO levels at axial position $z = 30D$ is obtained with ARC_22_GRI30, while ARC_22_GRI211 recovers correct values. This overprediction, almost by a factor of 2 close to the central region is consistent with previous observations [24] and with the differences observed in terms
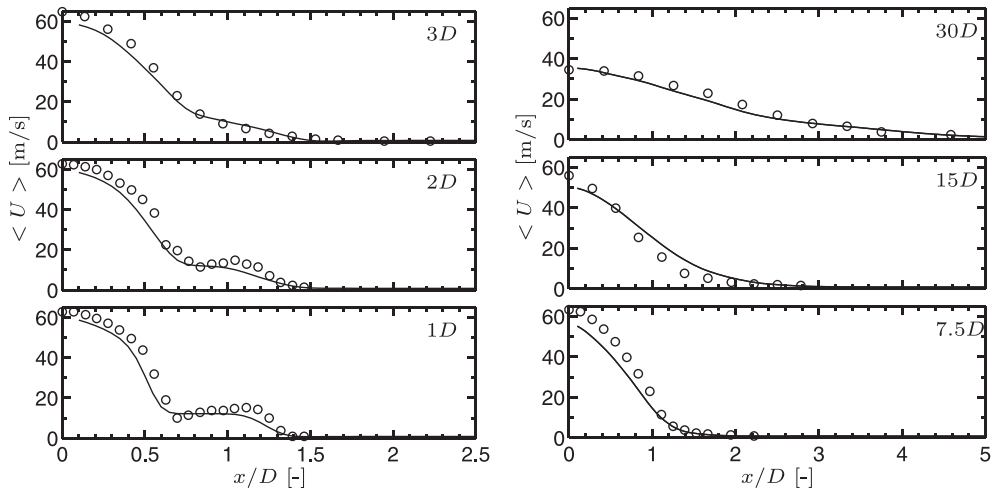
Fig. 8. Sandia flame D. Radial profiles of mean axial velocity at several axial positions. ARC_22 (-), Experimental data (○).
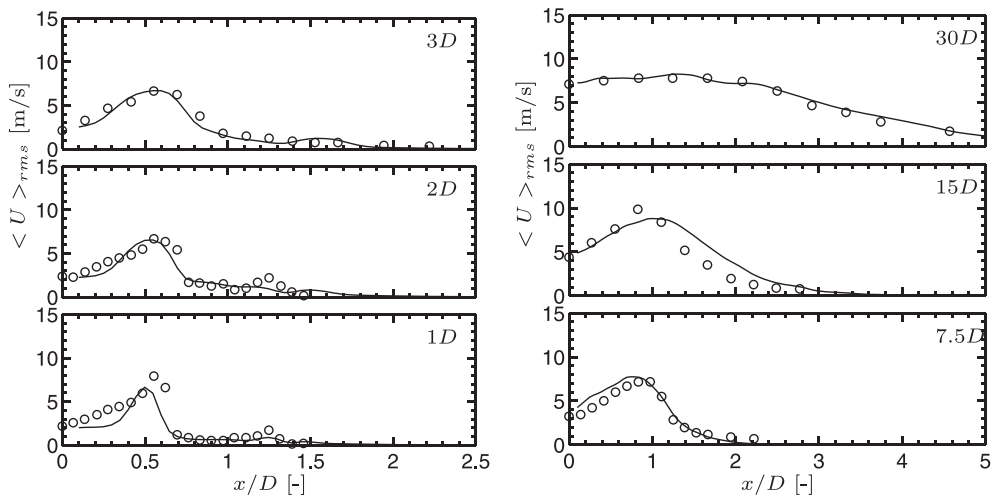
Fig. 9. Sandia flame D. Radial profiles of axial rms velocity at several axial positions. ARC_22 (-), Experimental data (○).

(a) Mixture fraction.
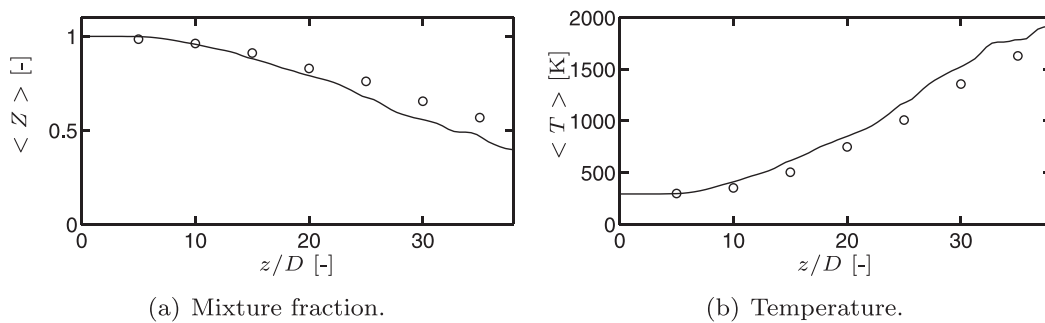
(b) Temperature.

Fig. 10. Sandia flame D. Axial profiles of a) mean mixture fraction and b) temperature. ARC_22 (-), Experimental data (○).

of NO production between the two versions of the mechanism on the laminar cases. This clearly emphasises the impact of kinetics on pollutant prediction, thus the choice of the detailed mechanism might be the most sensitive sub-model in the simulation for pollutant prediction. As significantly better results are obtained with ARC_22_GRI211, only this reduced mechanism is considered for the analysis of the flame structure that follows.

4.4. Analysis of the flame structure

4.4.1. The limit burning regimes

In the turbulent flame, the fresh air of the coflow can mix with the hot air of the pilot prior to combustion. As a result, the fuel burns with a mix of fresh air and burnt gases, which significantly affects the flame structure. This situation can be represented by

(a) Rms mixture fraction.
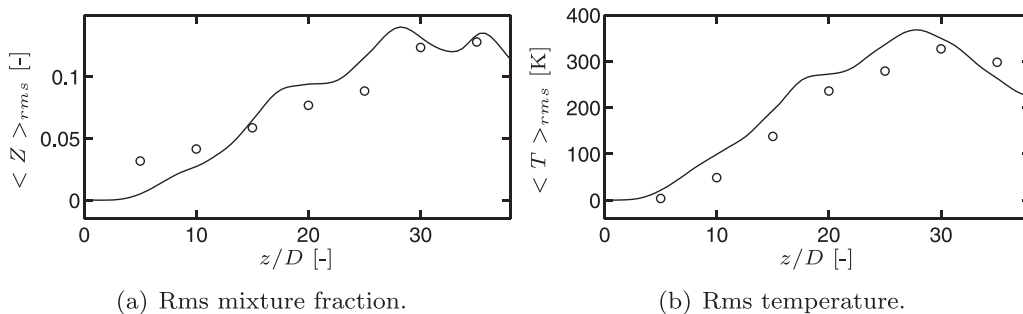
(b) Rms temperature.

Fig. 11. Sandia flame D. Axial profiles of a) rms mixture fraction and b) rms temperature. ARC_22 (-), Experimental data (○).
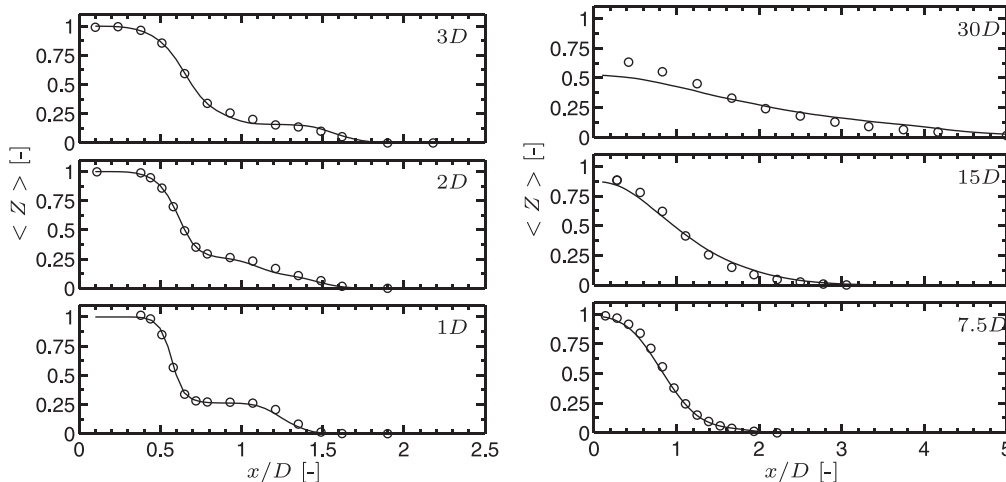
Fig. 12. Sandia flame D. Radial profiles of mean mixture fraction at several axial positions. ARC_22 (-), Experimental data (○).
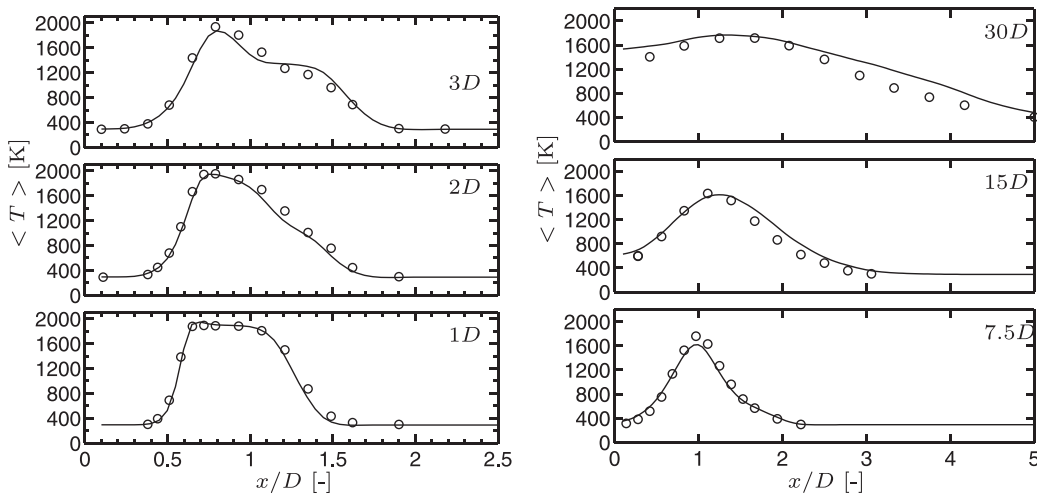
Fig. 13. Sandia flame D. Radial profiles of mean temperature at several axial positions. ARC_22 (-), Experimental data (○).

two series of counterflow strained flamelets, corresponding to the two extreme situations where the fuel burns with the coflow or pilot only:

- In the first series, the fuel burns with the coflow, with no impact of the pilot jet: the conditions of the coflow jet are imposed on one side and the conditions of the main central jet on the other side: this corresponds to the coflow flamelet series described in Section 3.2.

- In the second series, named pilot flamelet series hereafter, the pilot jet conditions replace the coflow ones, thus allowing to evaluate the influence of the pilot jet on the flame structure.

The response of the different mechanisms to scalar dissipation rate is shown in Fig. 17 for the pilot flamelet series. The coflow result are also included in Fig. 17 for comparison purposes. An excellent agreement is again obtained between ARC_22_GRI211 and GRI 2.11 in terms of maximum flame temperature, total fuel consumption, and CO production. For total NO production, a

(a) CO mass fraction.
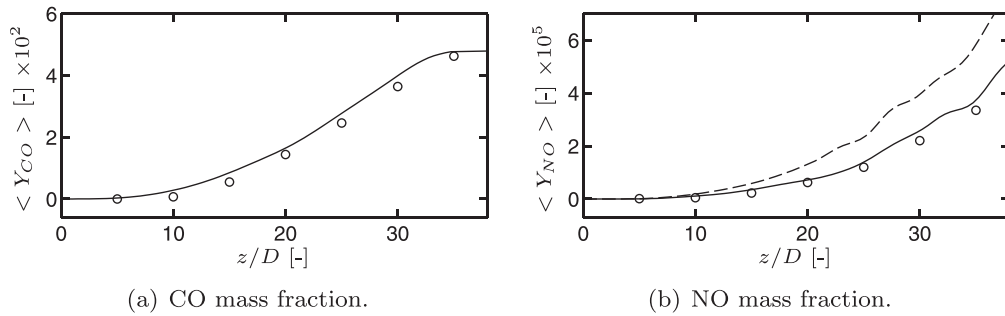
(b) NO mass fraction.

Fig. 14. Sandia flame D. Axial profiles along the centerline of a) mean CO mass fraction for ARC_22s (—) and b) NO mass fraction for ARC_22_GRI211 (—) and ARC_22_GRI30 (– –). Experimental data (○).
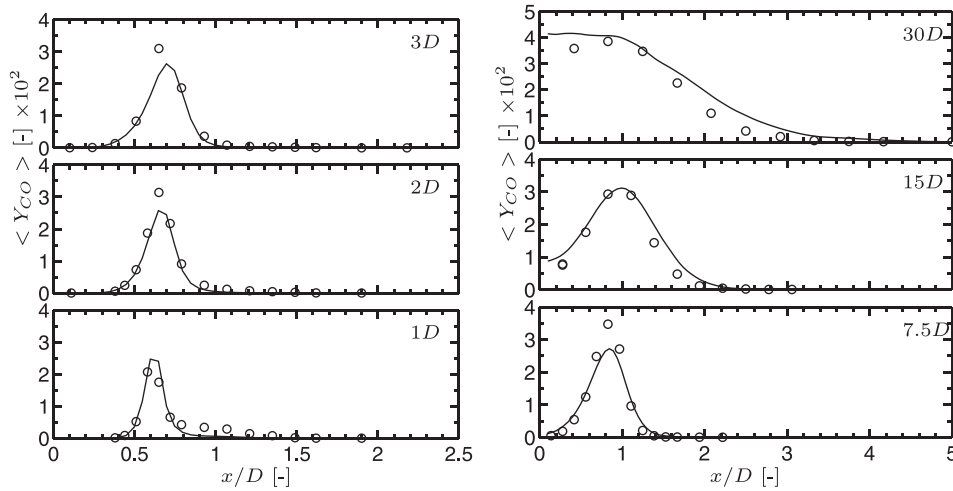
Fig. 15. Sandia flame D. Radial profiles of mean CO mass fraction at several axial positions. ARC_22 (-), Experimental data (○).
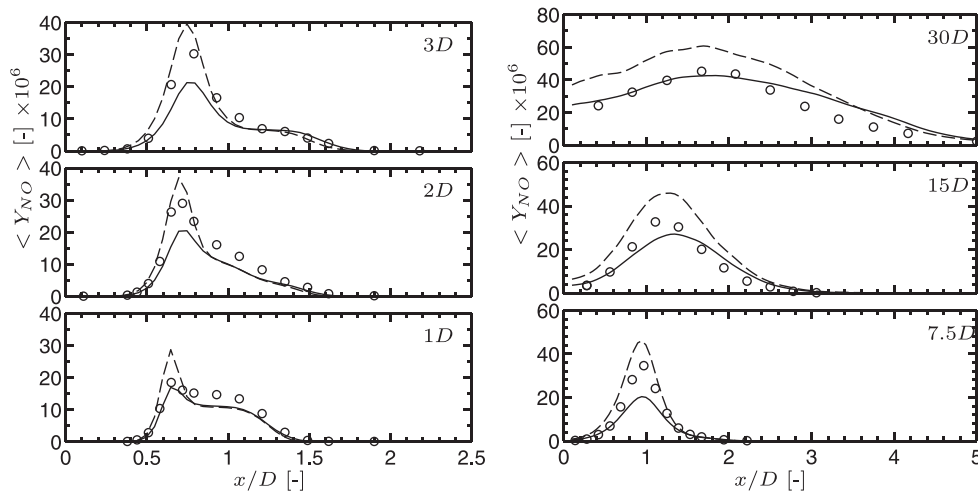
Fig. 16. Sandia flame D. Radial profiles of mean NO mass fraction at several axial positions. ARC_22_GRI211 (-), ARC_22_GRI30 (– –), Experimental data (○).

satisfactory agreement is obtained, with a maximum deviation of 15% around $\chi = 100$ s^{-1}.

It appears that the pilot flamelet series differs significantly from the coflow series. The maximum temperature (Fig. 17(a)) is higher and decreases less rapidly with scalar dissipation rate for the pilot flamelet series. The rapid decrease for the coflow flamelet series for high strain values indicates that the extinction limit is reached around $\chi = 450$ s^{-1}. For the pilot series, the feeding with hot products indeed promotes combustion at high scalar dissipa-

tion rates and delays extinction. However for scalar dissipation rates higher than $\chi = 650$ s^{-1}, the maximum temperature reaches a plateau value corresponding to the pilot inlet temperature, and only residual burning occurs, indicated by the very low total fuel consumption rate values in Fig. 17(b).

The CO production shown in Fig. 17(c) also differs significantly between the two series, as it is much higher for the pilot flamelet series. Surprisingly, the total NO production is similar for both flamelet series, despite their very different temperature level.

(a) Maximum temperature.

(b) Total fuel consumption.

(c) Total CO production.

(d) Total NO production.
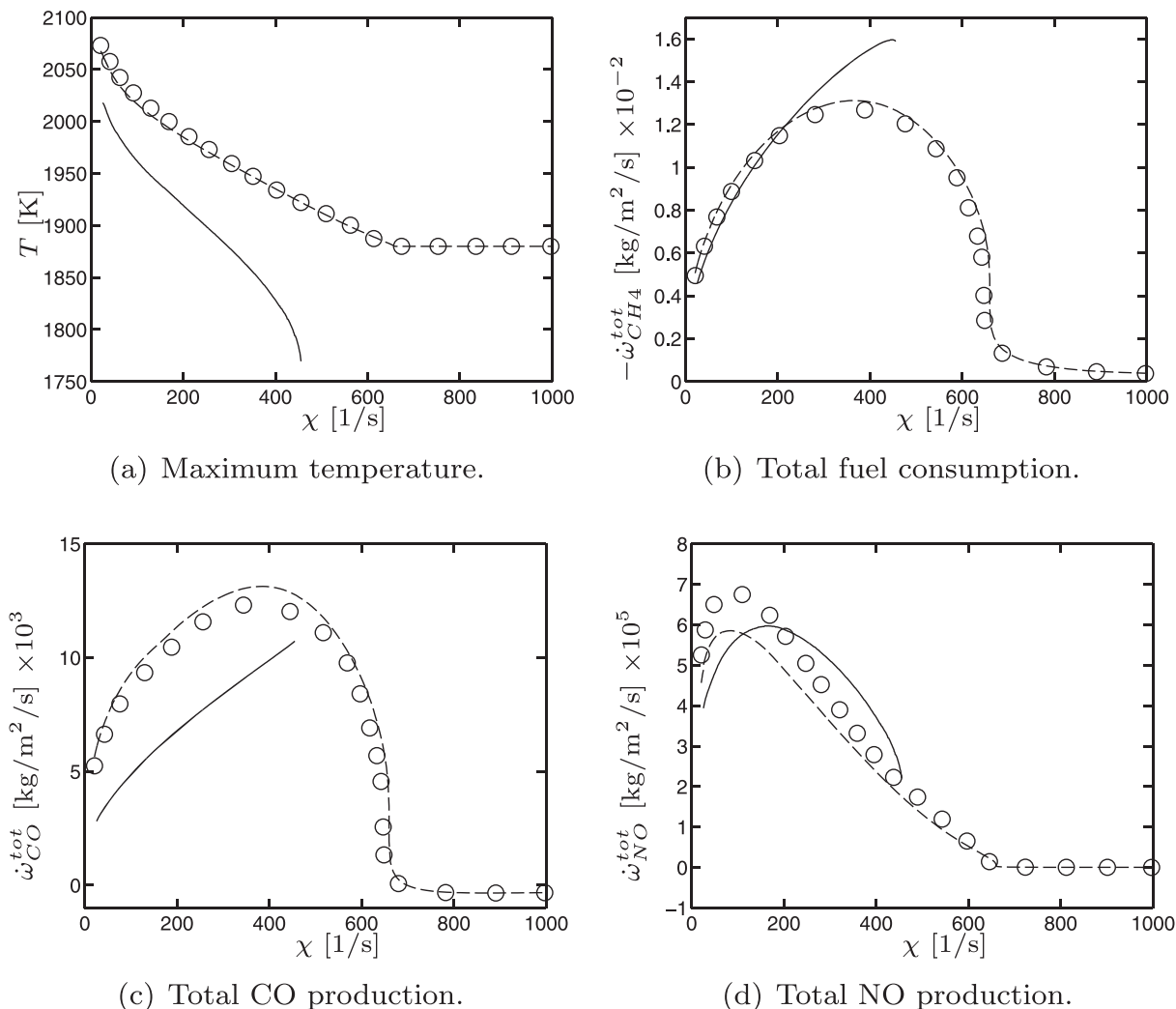
Fig. 17. Comparison of coflow and pilot counterflow flames in terms of a) maximum temperature, b) total CH_4 consumption rate, c) total CO production rate and d) total NO production rate. Pilot counterflow flames: GRI 2.11 (−−) and ARC_22_GRI211 (○). Coflow counterflow flames: ARC_22_GRI211 (−).

To better understand this behaviour, the flame structures in mixture fraction space are compared in Fig. 18 between the two flamelet series for two scalar dissipation rate values: $\chi = 90$ s^{-1}, corresponding to typical values found in the target turbulent flame, and $\chi = 400$ s^{-1}, which is close to the extinction limit ($\chi = 450$ s^{-1}) of the coflow series. Two general observations can be made: first the lean branch disappears in the pilot flame, and second, the hotter injection temperature of the pilot jet shifts the reaction zone toward the lean side, as highlighted by the location of CH_4, CO, and NO source terms. When comparing with the coflow flamelets, a direct consequence is that the CO consumption on the lean side cannot occur in the pilot flames (Fig. 18(c)), leading to a higher CO total production rate. Conversely, NO formation is less impacted by the presence of the pilot; its source term distribution remains similar, with production around stoichiometric mixture fraction and destruction on the rich side for both pilot and coflow flame series.

4.4.2. Burning regime of the turbulent flame

Laminar cases (Section 4.4.1) showed a high sensitivity of the flame structure to the scalar dissipation rate and to the burning conditions (coflow or pilot). To analyse the turbulent flame structure, scatter plots of several quantities as functions of the mixture fraction are extracted at axial locations $z = 7.5D$ and $z = 30D$. The

ARC_22_GRI211 scheme is retained for the analysis, since it overall yields the most satisfactory results. Statistics conditioned on mixture fraction are extracted from LES and compared with experimental data and with counterflow laminar flames, at a scalar dissipation rate corresponding to the mean value observed in the LES ($\chi = 105$ s^{-1} and 75 s^{-1} at $z = 7.5D$ and $30D$ respectively).

At location $z = 7.5D$ (Fig. 19), the temperature distribution in Z-space is typical of a turbulent non-premixed flame (Fig. 19(a)), with moderate rms fluctuations (denoted by the error bars) around the mean temperature profile, due to scalar dissipation rate fluctuations. An excellent agreement is obtained with the experimental results in terms of conditional mean and rms temperature, although the temperature dispersion in the rich core ($Z > 0.6$) is not fully captured. The mean temperature distribution is close to the two reference flamelets, which confirms the non-premixed flame structure at this location.

Figure 19(b) shows the conditional mean and rms OH mass fraction. The peak value in the reaction zone and the fluctuation levels are well reproduced. Again, the distribution is close to the two reference flamelets, even if there is a strong departure from the pilot flamelet on the lean side. It is attributed to the zero OH mass fraction imposed on the oxidiser side for the pilot series. The conditional mean and rms CO and NO mass fractions are shown in Fig. 19(c) and Fig. 19(d) respectively, and are again in good

(a) Temperature.

(b) CH$_4$ destruction rate.

(c) CO source term.
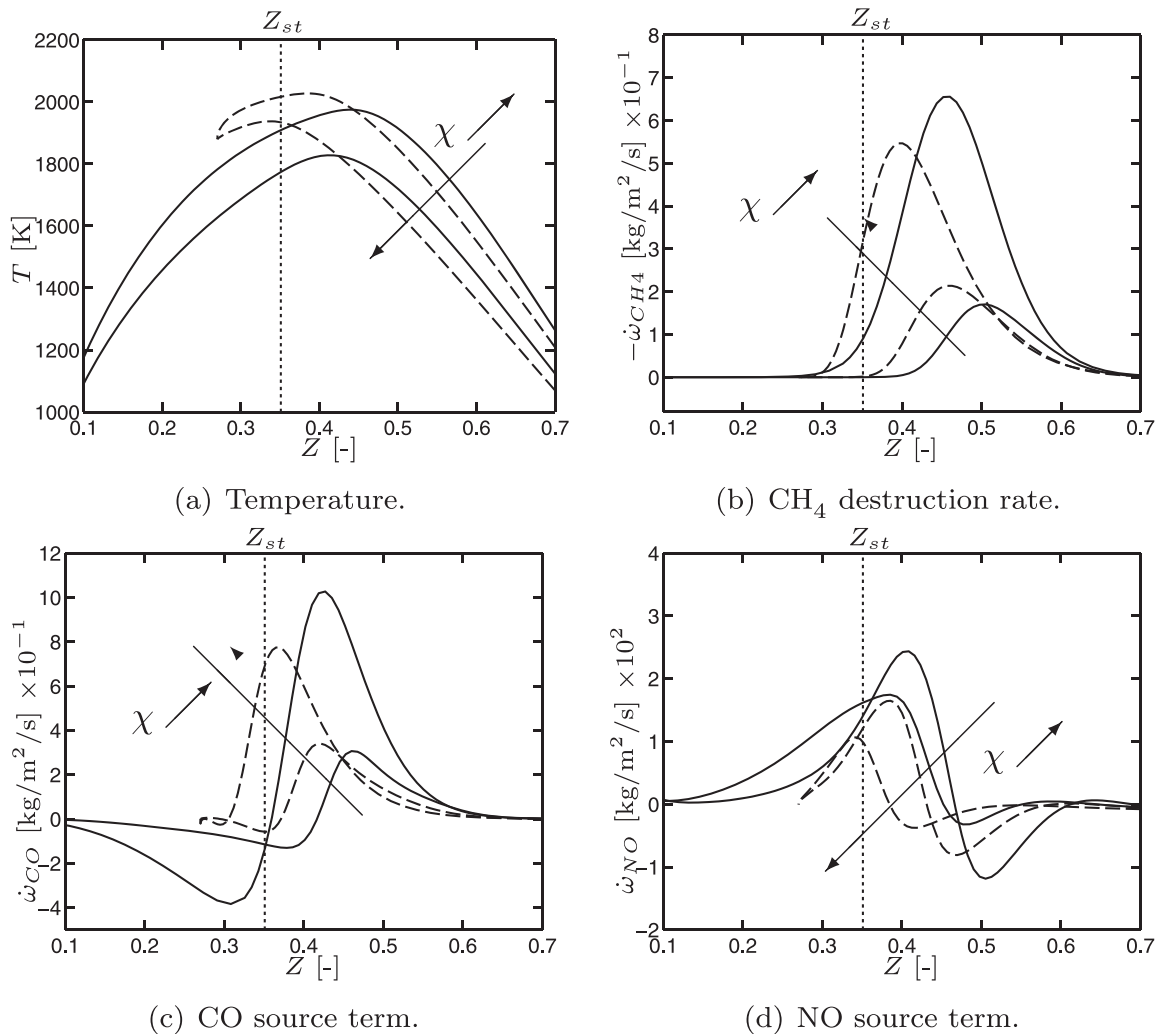
(d) NO source term.

Fig. 18. Laminar counterflow flames with ARC_22_GRI211. a) Temperature, b) CH$_4$ destruction rate, c) CO source term and d) NO source term vs mixture fraction. Comparison of coflow (—) and pilot (−−) counterflow flames at scalar dissipation rates $\chi = 90$ s^{-1} and 400 s^{-1}.

agreement with the experimental distributions, although NO mass fraction is globally slightly underpredicted, consistently with the NO radial profiles of Fig. 16. Both CO and NO peak at rich conditions around $Z \simeq 0.4$. On the lean side, CO is rapidly oxidised to CO$_2$, leading to a sharp decrease of CO mass fraction. Once again, both coflow and pilot laminar flame structures are consistent with the distributions of CO and NO.

Very similar results are obtained downstream at axial position $z = 30D$, as shown in Fig. 20 for temperature, OH, CO, and NO mass fractions. Again LES conditional data are in good qualitative agreement with the experiment, the global shape, mean levels, and dispersion being rather well captured. Note that the mean scalar dissipation rate extracted from LES is lower in this case ($\chi = 75$ s^{-1} compared to 105 s^{-1} at $z = 7.5D$). The turbulent flame structure is still consistent with the reference flamelets, except for NO mass fraction which departs from the pilot flamelets. The imposed value for NO on the pilot side in flamelet calculations is $Y_{NO} = 2 \times 10^{-5}$, which corresponds to the composition imposed at the pilot jet inlet in the LES. This value yields a good agreement between the pilot flamelets and the turbulent flame at axial location $z = 7.5D$. However, NO concentrations increase with axial position as NO is produced in the flame. Thus the levels observed in the turbulent flame are higher ($Y_{NO} \simeq 5 \times 10^{-5}$) at $z = 30D$ than the boundary

value used for flamelet calculations, which explains the discrepancy observed for NO mass fraction.

To evaluate quantitatively the impact of the pilot on the response of the turbulent flame to scalar dissipation rate, CH$_4$ source term and scalar dissipation rate are extracted along a $Z = 0.4$ iso-surface from an instantaneous LES field, at two locations: the first in the vicinity of $z = 7.5D$ plane (between $7.5D$ and $10D$) and the second close to $z = 30D$ plane (between $30D$ and $33D$). The distribution of CH$_4$ source term is compared for the two axial locations in Fig. 21. Statistics conditioned on the local scalar dissipation rate are also shown and provide an estimate of the local mean and dispersion. A first observation is that the data dispersion is very large, especially at high scalar dissipation rate values ($\chi > 200$ s^{-1}), with significant non-quenched flame points at scalar dissipation rates significantly beyond the extinction limit at location $z = 7.5D$. This may be attributed to the unsteady flame response to scalar dissipation rate fluctuations [36,40]. A second observation is that, despite this dispersion, a clear trend can be observed for the fuel source term conditional mean: fuel consumption tends to have a bi-modal behaviour, with data points distributed either around the pilot or the coflow flamelet response curves. This is especially visible at low scalar dissipation rate values. Overall, the flame response is found to be in good agreement with the pilot flamelets at $z = 7.5D$

(a) Temperature.

(b) OH mass fraction.

(c) CO mass fraction.
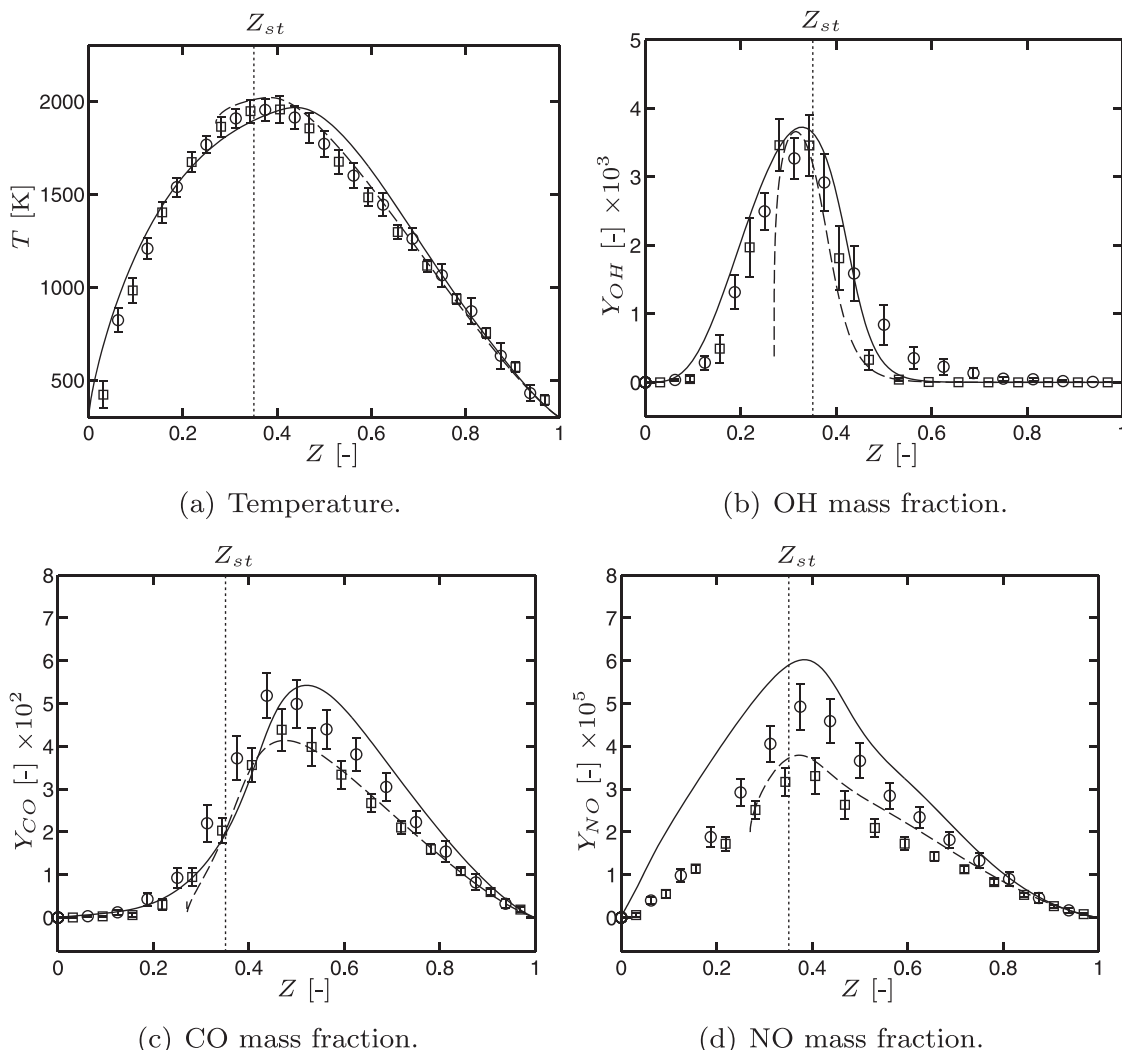
(d) NO mass fraction.

Fig. 19. Sandia flame D. Conditional mean (symbols) and rms (error bars) temperature, OH, CO and NO mass fractions vs mixture fraction at axial location $z = 7.5D$. Comparison between LES ($\square$) and experiments ($\circ$). Coflow counterflow flame (—) and pilot counterflow flame (−−) at the mean scalar dissipation rate from LES $\chi = 105$ s^{-1}.

and with the coflow flamelets at $z = 30D$. This supports the strong influence of the pilot at locations close to the jet exits.

This behaviour is well supported by the distribution of the scalar dissipation rate in Z-space shown in Fig. 22. Once again, the dispersion is very large because of unsteady effects, but the evolution of the conditional mean scalar dissipation rate structure in mixture fraction space from $z = 7.5D$ to $z = 30D$ is consistent with the previous observations: at $z = 7.5D$ (Fig. 22(a)), the peak of scalar dissipation rate is located around $Z = 0.5$, similarly to the pilot reference flamelet; at $z = 30D$, the scalar dissipation rate is globally lower, with a peak value around $Z = 0.4$ which is consistent with the coflow reference flamelet.

From the analysis of the CH$_4$ source term response to scalar dissipation rate and scalar dissipation rate structure, and in light of the laminar cases, it can be concluded that the turbulent flame does not exhibit a single canonical structure. The coflow and pilot counterflow flamelet series correspond to two limit burning regimes of the main jet, with either pure air of the coflow (coflow regime) or lean burnt gases of the pilot (pilot regime). Close to injection, at $z = 7.5D$, the good agreement with the pilot flamelets indicates that the pilot regime is dominant in this zone. Conversely, at downstream locations, the effect of the pilot, which represents only a 1/5 of the main central injection mass flow rate,

is expected to be weaker. This assertion is supported by the fuel source term response observed at $z = 30D$, which correlates best with coflow flamelets, and by the change in scalar dissipation rate structure, thus indicating that the flame burns dominantly in a coflow regime in this region.

4.4.3. Implications for pollutant formation

This composite flame structure is expected to have a significant impact on pollutant formation, as suggested by the laminar cases of Section 4.4.1. Similarly to the analysis performed for the fuel consumption rate, CO and NO source term responses to scalar dissipation are extracted at the same two axial locations. The CO source term response shown in Fig. 23 reveals again a behaviour consistent with pilot flamelets at $z = 7.5D$ and coflow flamelets at $z = 30D$. This leads to a strong change of the CO source term at the selected mixture fraction ($Z = 0.4$), with CO destruction from the coflow regime, and conversely CO production in the pilot regime. This is also observed in the LES results, where both positive and negative source terms are found.

Finally the comparison of the NO source term with flamelets is shown in Fig. 24. In the same way, a very good correlation is observed for NO source term extracted from LES and the reference flamelets, up to $\chi \simeq 200$ s^{-1}: the conditional mean source term

(a) Temperature.

(b) OH mass fraction.

(c) CO mass fraction.
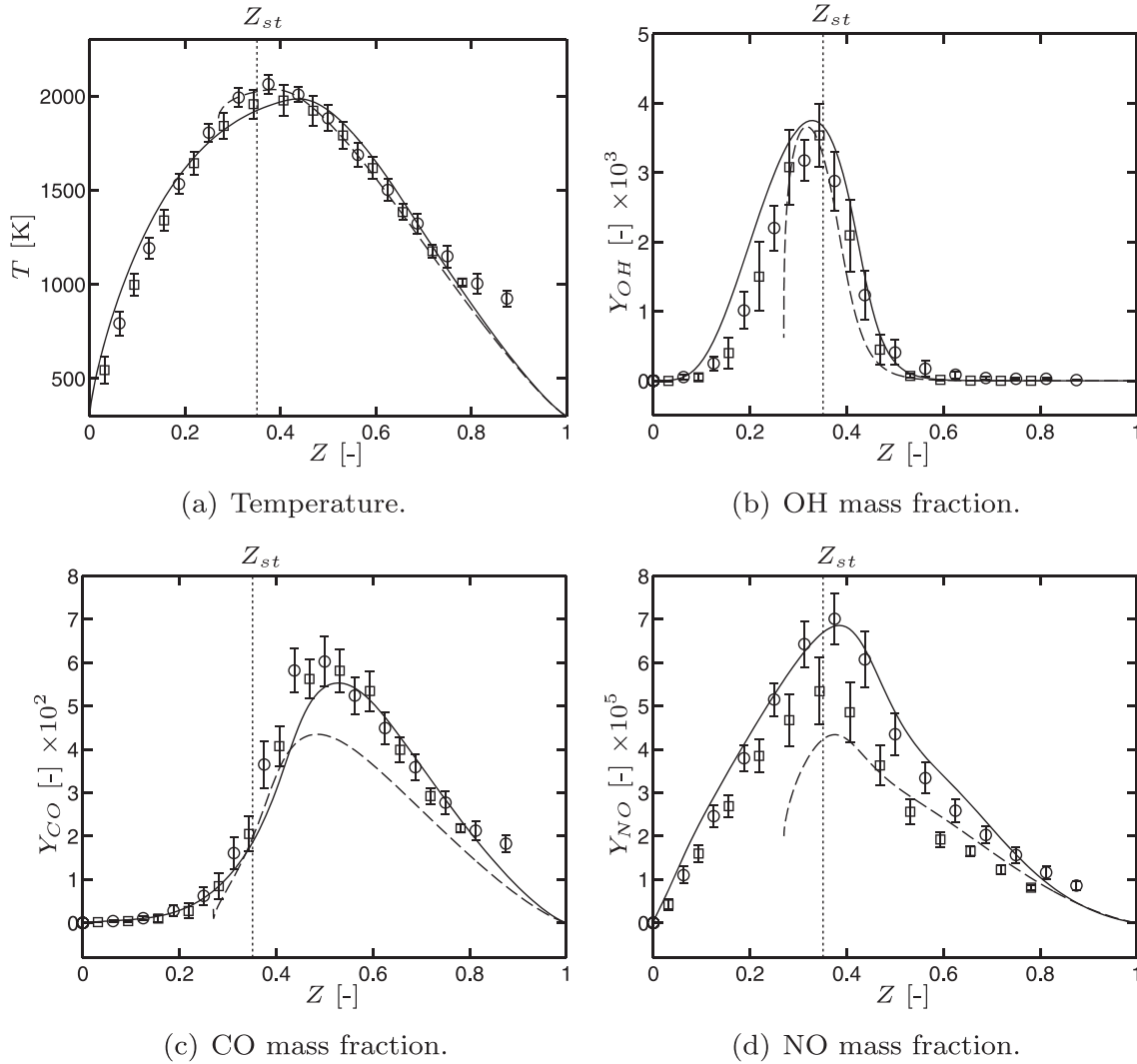
(d) NO mass fraction.

Fig. 20. Sandia flame D. Conditional mean (symbols) and rms (error bars) temperature, OH, CO and NO mass fractions vs mixture fraction at axial location $z = 30D$. Comparison between LES (□) and experiments (○). Coflow counterflow flame (−) and pilot counterflow flame (−−) at the mean scalar dissipation rate from LES $\chi = 75\,\text{s}^{-1}$.
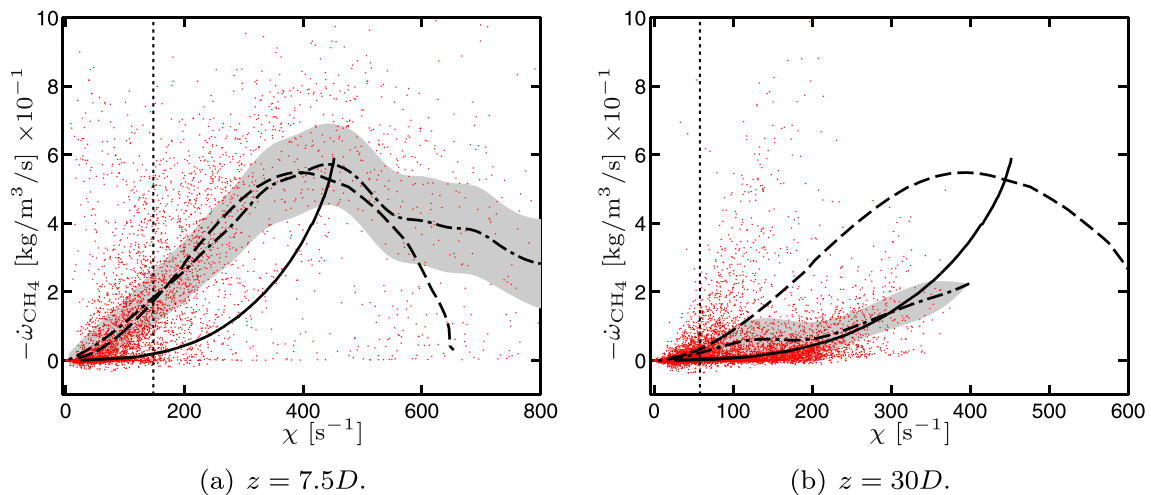
(a) $z = 7.5D$.

(b) $z = 30D$.

Fig. 21. Sandia flame D. Scatter plot of CH_4 consumption rate versus scalar dissipation rate along the $Z = 0.4$ isosurface at axial locations a) $z = 7.5D$ and b) $z = 30D$. The grey shaded area corresponds to the conditional standard deviation around the conditional mean ($\cdot - \cdot -$) of the scatter data. The vertical line corresponds to the mean scalar dissipation rate. LES results are compared to the coflow counterflow flamelets (−) and the pilot counterflow flamelets (−−).
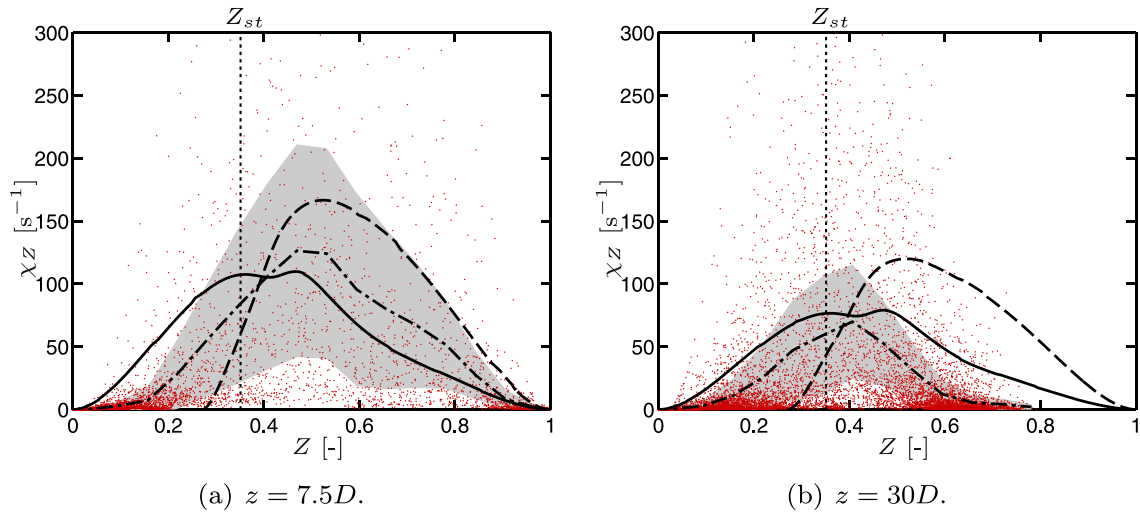
(a) $z = 7.5D$.   (b) $z = 30D$.

Fig. 22. Sandia flame D. Scatter plot of local scalar dissipation rate χ_Z versus mixture fraction at axial locations a) $z = 7.5D$ and b) $z = 30D$. The grey shaded area corresponds to the conditional standard deviation around the conditional mean ($\cdot - \cdot -$) of the scatter data. LES results are compared to the coflow counterflow flamelets (−) and the pilot counterflow flamelets (−−) at the mean scalar dissipation rate from LES.
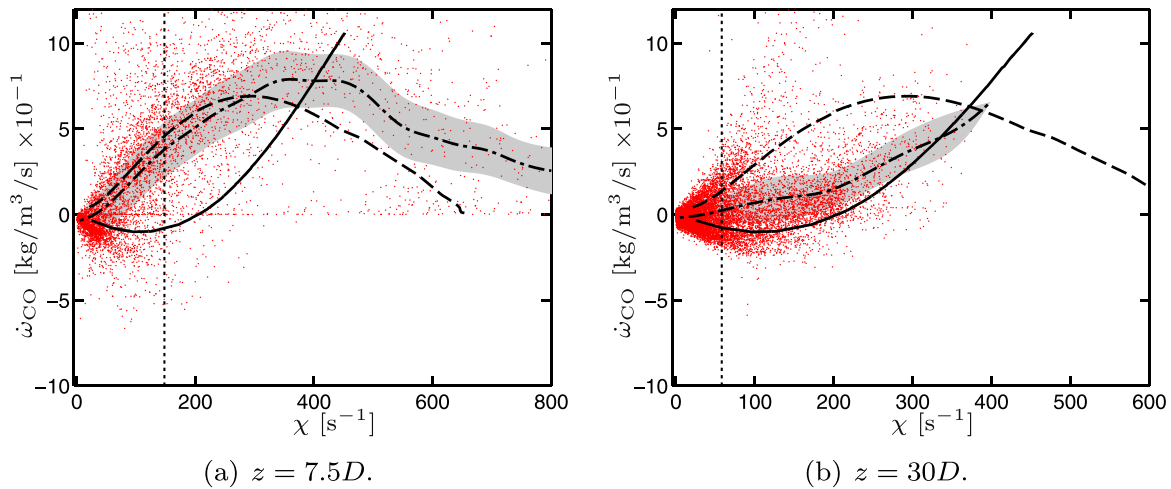
(a) $z = 7.5D$.   (b) $z = 30D$.

Fig. 23. Sandia flame D. Scatter plot of CO production rate versus scalar dissipation rate along the $Z = 0.4$ isosurface at axial locations a) $z = 7.5D$ and b) $z = 30D$. The grey shaded area corresponds to the conditional standard deviation around the conditional mean ($\cdot - \cdot -$) of the scatter data. The vertical line corresponds to the mean scalar dissipation rate. LES results are compared to the coflow counterflow flamelets (−) and the pilot counterflow flamelets (−−).
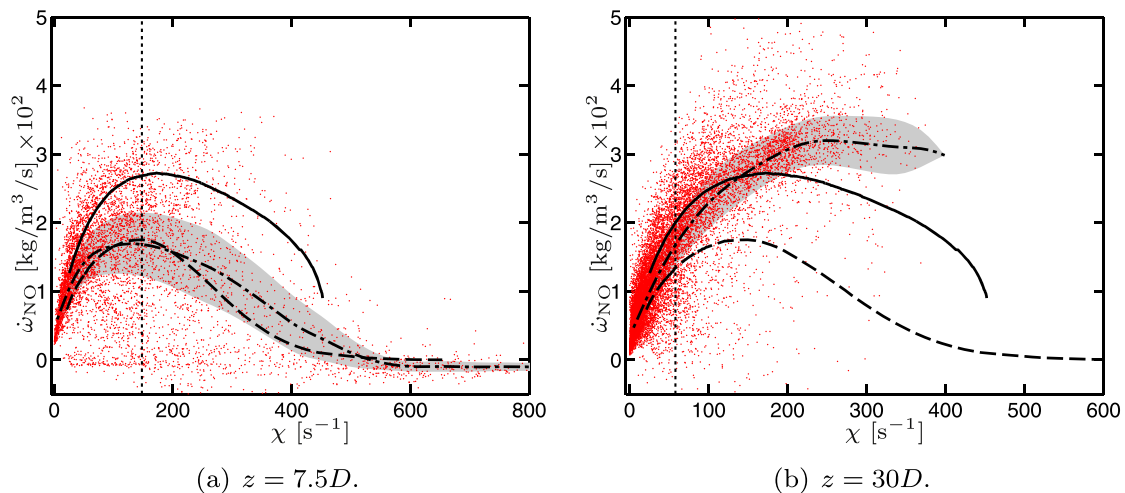
(a) $z = 7.5D$.   (b) $z = 30D$.

Fig. 24. Sandia flame D. Scatter plot of NO production rate versus scalar dissipation rate along the $Z = 0.4$ isosurface at axial locations a) $z = 7.5D$ and b) $z = 30D$. The grey shaded area corresponds to the conditional standard deviation around the conditional mean ($\cdot - \cdot -$) of the scatter data. The vertical line corresponds to the mean scalar dissipation rate. LES results are compared to the coflow counterflow flamelets (−) and the pilot counterflow flamelets (−−).

behaviour agrees well with the pilot flamelets at $z = 7.5D$ and with the coflow flamelets at $z = 30D$.

The pollutant formation is found to be largely consistent with the laminar reference flames. Therefore, it can be deduced from the laminar cases (Fig. 17(c)) that CO production is promoted in the turbulent flame at the first axial locations, where the pilot regime is dominant. On the other hand, as shown in Fig. 17(d), despite very different flame structure, NO production is not significantly impacted. The strong impact on CO might explain the unsatisfactory prediction of CO generally observed in tabulated chemistry models on this configuration [8], where in most cases, coflow flamelets were used to construct the look-up table. To improve the local description of the flame structure, an additional parameter describing the mixing state between the coflow and the pilot can be introduced, as done in [9]. However, the construction of this parameter may be difficult in turbulent flames.

5. Conclusions

In this paper, a highly resolved LES of the Sandia flame D has been performed with direct integration of realistic chemistry. Two ARCs based on the GRI 3.0 and GRI 2.11 detailed mechanisms have been employed in the simulations. The mixture fraction, temperature, and CO mass fraction profiles were shown to be in very good agreement with the experimental data. The slight discrepancies observed were essentially due to a slight over-prediction of the global mixing rate. Consistently with previous studies, strong disparities are observed between the reduced mechanisms based either on GRI 3.0 or GRI 2.11 for NO prediction. While a very satisfactory agreement of NO is obtained with GRI 2.11, the reduced mechanism based on GRI 3.0 leads to a significant overprediction of NO produced by the flame.

The approach used in this work, based on the direct integration of ARC chemistry allows a faithful representation of the flame structure and pollutant emissions. The analysis of the response to the local flow and mixing conditions in the turbulent flame showed that the burning mode is essentially non-premixed. The turbulent flame response to scalar dissipation rate is similar to counterflow diffusion flamelets, and exhibits a very large dispersion due to turbulent effects. A detailed analysis of the chemical source terms reveals two limit burning regimes, either controlled by the pilot or the coflow. Depending on the mixing between the two, the flame exhibits an intermediate structure between these two regimes. The pilot has a strong influence at the flame basis, which significantly impacts the flame structure and pollutant formation, leading in particular to a strong increase of CO formation. This implies that the turbulent flame cannot be accurately described by a unique reference flamelet, and suggests that various levels of mixing between the fuel jet, pilot and air co-flow should be incorporated in a flamelet table to properly recover the flame structure.

The computational cost of ARC was found to represent only a fraction of the total computation cost. Properly coupled with a subgrid turbulent combustion model for LES, ARCs represent therefore a promising modelling strategy for chemistry in more complex industrial configurations [15,18], in which capturing a detailed flame structure is critical to reproduce various phenomena such as pollutant emissions, but also autoignition, heat losses or two-phase flow effects.

Acknowledgments

References

[1] Y.B. Zeldovich, The oxidation of nitrogen in combustion and explosions, Acta Physicochim. URSS 21 (4) (1946) 218.

[2] P.C. Malte, D.T. Pratt, The role of energy-releasing kinetics in NOx formation: fuel-lean, jet-stirred CO–air combustion, Combust. Sci. Technol. 9 (5–6) (1974) 221–231.

[3] S.M. Correa, A review of NOx formation under gas–turbine combustion conditions, Combust. Sci. Technol. 87 (1–6) (1993) 329–362.

[4] C.P. Fenimore, Formation of nitric oxide in premixed hydrocarbon flames, Symp. (Int.) Combust. 13 (1) (1971) 373–380.

[5] T.C. Lieuwen, V. Yang, Gas turbine emissions, Cambridge University Press, 2013.

[6] R.S. Barlow, J.H. Frank, Effects of turbulence on species mass fractions in methane/air jet flames, Symp. (Int.) Combust. 27 (1) (1998) 1087–1095.

[7] F. Pecquery, V. Moureau, G. Lartigue, L. Vervisch, A. Roux, Modelling nitrogen oxide emissions in turbulent flames with air dilution: application to LES of a non-premixed jet-flame, Combust. Flame 161 (2) (2014) 496–509.

[8] A.W. Vreman, B.A. Albrecht, J.A. van Oijen, L.P.H. de Goey, R.J.M. Bastiaans, Premixed and nonpremixed generated manifolds in large-eddy simulation of Sandia flame D and F, Combust. Flame 153 (3) (2008) 394–416.

[9] C. Locci, O. Colin, D. Poitou, F. Mauss, A tabulated, flamelet based no model for large eddy simulations of non premixed turbulent jets with enthalpy loss, Flow, Turb. Combust. 94 (4) (2015) 691–729.

[10] M. Ihme, H. Pitsch, Modeling of radiation and nitric oxide formation in turbulent nonpremixed flames using a flamelet/progress variable formulation, Phys. Fluids 20 (5) (2008) 055110–055110–20.

[11] B.T. Zoller, J.M. Allegrini, U. Maas, P. Jenny, PDF model for NO calculations with radiation and consistent NO–NO$_2$ chemistry in non-premixed turbulent flames, Combust. Flame 158 (8) (2011) 1591–1601.

[12] C.J. Sung, C.K. Law, J.Y. Chen, Augmented reduced mechanisms for NO emission in methane oxidation, Combust. Flame 125 (1–2) (2001) 906–919.

[13] T. Lu, C.K. Law, A criterion based on computational singular perturbation for the identification of quasi steady state species: a reduced mechanism for methane oxidation with NO chemistry, Combust. Flame 154 (4) (2008) 761–774.

[14] W.P. Jones, V.N. Prasad, Large Eddy simulation of the Sandia flame series (D-F) using the Eulerian stochastic field method, Combust. Flame 157 (9) (2010) 1621–1636.

[15] G. Bulat, W.P. Jones, A.J. Marquis, NO and CO formation in an industrial gas-turbine combustion chamber using LES with the Eulerian sub-grid PDF method, Combust. Flame 161 (7) (2014) 1804–1825.

[16] S. Navarro-Martinez, A. Kronenburg, LES-CMC simulations of a lifted methane flame, Proc. Combust. Inst. 32 I (2009) 1509–1516.

[17] B. Franzelli, E. Riber, B. Cuenot, Impact of the chemical description on a large Eddy simulation of a lean partially premixed swirled flame, C. R. Mecanique 341 (1–2) (2013) 247–256.

[18] T. Jaravel, E. Riber, B. Cuenot, G. Bulat, Large Eddy simulation of an industrial gas turbine combustor using reduced chemistry with accurate pollutant prediction, Proc. Combust. Inst. 36 (3) (2017) 3817–3825.

[19] O. Schulz, T. Jaravel, T. Poinsot, B. Cuenot, N. Noiray, A criterion to distinguish autoignition and propagation applied to a lifted methane–air jet flame, Proc. Combust. Inst. 36 (2) (2017) 1637–1644.

[20] C.T. Bowman, R.K. Hanson, D.F. Davidson, W.C.G. Jr., V. Lissianski, G.P. Smith, D.M. Golden, M. Frenklach, M. Goldenberg, GRI-Mech 2.11, 1995.

[21] C.T. Bowman, M. Frenklach, W.R. Gardiner, G. Smith, The GRI 3.0 chemical kinetic mechanism, 1999.

[22] A.A. Konnov, Implementation of the NCN pathway of prompt-NO formation in the detailed reaction mechanism, Combust. Flame 156 (11) (2009) 2093–2105.

[23] N. Lamoureux, P. Desgroux, A. El Bakali, J.F. Pauwels, Experimental and numerical study of the role of NCN in prompt-NO formation in low-pressure CH$_4$-O$_2$-N$_2$ and C$_2$H$_2$-O$_2$-N$_2$ flames, Combust. Flame 157 (10) (2010) 1929–1941.

[24] R.R. Cao, S.B. Pope, The influence of chemical mechanisms on PDF calculations of nonpremixed piloted jet flames, Combust. Flame 143 (4) (2005) 450–470.

[25] R.S. Barlow, A.N. Karpetis, J.H. Frank, J.Y. Chen, Scalar profiles and NO formation in laminar opposed-flow partially premixed methane/air flames, Combust. Flame 127 (3) (2001) 2102–2118.

[26] P. Pepiot, Automatic strategies to model transportation fuel surrogates, Stanford University, 2008 Ph.D. thesis.

[27] P. Pepiot-Desjardins, H. Pitsch, An efficient error-propagation-based reduction method for large chemical kinetic mechanisms, Combust. Flame 154 (1–2) (2008) 67–81.

[28] T. Lu, C.K. Law, C.S. Yoo, J.H. Chen, Dynamic stiffness removal for direct numerical simulations, Combust. Flame 156 (8) (2009) 1542–1551.

[29] T. Lovas, P. Amnéus, F. Mauss, E. Mastorakos, Comparison of automatic reduction procedures for ignition chemistry, Proc. Combust. Inst. 29 (1) (2002) 1387–1393.

[30] T. Lovas, D. Nilsson, F. Mauss, Automatic reduction procedure for chemical mechanisms applied to premixed methane/air flames, Proc. Combust. Inst. 28 (2) (2000) 1809–1815.

[31] B. Fiorina, O. Gicquel, L. Vervisch, S. Carpentier, N. Darabiha, Approximating the chemical structure of partially premixed and diffusion counterflow flames using FPI flamelet tabulation, Combust. Flame 140 (3) (2005) 147–160.

[32] O. Colin, M. Rudgyard, Development of high-order Taylor–Galerkin schemes for LES, J. Comput. Phys. 162 (2) (2000) 338–371.

[33] T.J. Poinsot, S.K. Lele, Boundary conditions for direct simulations of compressible viscous flows, J. Comput. Phys. 101 (1) (1992) 104–129.

[34] S.B. Pope, Turbulent flows, 1, Cambridge University Press, 2000.

[35] F. Nicoud, H.B. Toda, O. Cabrit, S. Bose, J. Lee, Using singular values to build a subgrid-scale model for Large Eddy Simulations, Phys. Fluids 23 (8) (2011).

[36] H.G. Im, J.H. Chen, J.Y. Chen, Chemical response of methane/air diffusion flames to unsteady strain rate, Combust. Flame 118 (1–2) (1999) 204–212.

[37] B. Cuenot, T. Poinsot, Effects of curvature and unsteadiness in diffusion flames. Implications for turbulent diffusion combustion, Symp. (Int.) Combust. 25 (1) (1994) 1383–1390.

[38] P. Schmitt, T. Poinsot, B. Schuermans, K.P. Geigle, Large-eddy simulation and experimental study of heat transfer, nitric oxide emissions and combustion instability in a swirled turbulent high-pressure burner, J. Fluid Mech. 570 (2007) 17.

[39] K.A. Kemenov, S.B. Pope, Molecular diffusion effects in LES of a piloted methane–air flame, Combust. Flame 158 (2) (2011) 240–254.

[40] J.M. Donbar, J.F. Driscoll, C.D. Carter, Reaction zone structure in turbulent non-premixed jet flames - from CH–OH PLIF images, Combust. Flame 122 (1–2) (2000) 1–19.